The scaffolding protein ZO-1 coordinates actomyosin and epithelial apical specializations *in vitro* and *in vivo*

Received for publication, May 9, 2018, and in revised form, September 14, 2018 Published, Papers in Press, September 21, 2018, DOI 10.1074/jbc.RA118.003908

Matthew A. Odenwald[‡], Wangsun Choi[§], Wei-Ting Kuo[§], Gurminder Singh[‡§], Anne Sailer[‡], Yitang Wang[‡], Le Shen[‡¶], Alan S. Fanning[‖], and Jerrold R. Turner[‡§1]

From the Departments of [‡]Pathology and [¶]Surgery, University of Chicago, Chicago, Illinois 60637, the [§]Department of Pathology, Brigham and Women's Hospital and Harvard Medical School, Boston, Massachusetts 02115, and the [‖]Department of Cell Biology and Physiology, University of North Carolina, Chapel Hill, North Carolina 27599

Edited by Velia M. Fowler

Polarized epithelia assemble into sheets that compartmentalize organs and generate tissue barriers by integrating apical surfaces into a single, unified structure. This tissue organization is shared across organs, species, and developmental stages. The processes that regulate development and maintenance of apical epithelial surfaces are, however, undefined. Here, using an intestinal epithelial-specific knockout (KO) mouse and cultured epithelial cells, we show that the tight junction scaffolding protein zonula occludens-1 (ZO-1) is essential for development of unified apical surfaces *in vivo* and *in vitro*. We found that U5 and GuK domains of ZO-1 are necessary for proper apical surface assembly, including organization of microvilli and cortical F-actin; however, direct interactions with F-actin through the ZO-1 actin-binding region (ABR) are not required. ZO-1 lacking the PDZ1 domain, which binds claudins, rescued apical structure in ZO-1–deficient epithelia, but not in cells lacking both ZO-1 and ZO-2, suggesting that heterodimerization with ZO-2 restores PDZ1-dependent ZO-1 interactions that are vital to apical surface organization. Pharmacologic F-actin disruption, myosin II motor inhibition, or dynamin inactivation restored apical epithelial structure *in vitro* and *in vivo*, indicating that ZO-1 directs epithelial organization by regulating actomyosin contraction and membrane traffic. We conclude that multiple ZO-1–mediated interactions contribute to coordination of epithelial actomyosin function and genesis of unified apical surfaces.

Epithelial surfaces are composed of sheets of polarized cells. In these, the basolateral surfaces attach to adjacent cells and the underlying basement membrane, whereas apical surfaces interface directly with the extracellular (*e.g.* luminal) milieu. Apical specializations, including microvilli and cilia, vary by organ and cell type, but a constant feature of apical membranes is their precise integration to form a single, contiguous surface in which it can be difficult to identify boundaries between individual cells. This organization, which presents a united front to pathogens and other external stressors (1), is thermodynamically unfavorable (2, 3) and must, therefore, require energy expenditure and be functionally important. Nevertheless, the mechanisms by which contiguous cell populations establish and maintain uniform apical surfaces have not been defined.

Even in the first stages of multicellular organism development, individual epithelial cells integrate to form a uniform apical surface; this structure is maintained during dynamic tissue processes. As early as embryo invagination, the apical surface of polarized epithelia undergoes constriction, in which the apical actomyosin network contracts to decrease cross-sectional apical surface area while maintaining continuous apical surfaces (4–11). In developing murine intestinal epithelia, uniform apical surfaces are maintained during progression through transient pseudostratified structures (12). At the other end of the spectrum, apical borders are maintained during epithelial cell extrusion until the point where the cell being shed extends beyond adjacent cells (13–16). In contrast, this tissue organization is lost in early neoplasia and when intercellular junctions are disrupted.

Direct interactions between F-actin and zonula occludens-1 (ZO-1)[2] have been implicated in a number of coordinated cellular processes, including tissue morphogenesis, maintenance of apical structure, and barrier regulation (17–19). To better define the contributions of these and other ZO-1–mediated interactions to epithelial organization, we generated intestinal epithelial-specific ZO-1 knockout (KO) mice. Apicobasal polarity of these epithelia was maintained, but apical membranes formed convex surfaces that disrupted apical surface continuity. Similar defects were present in ZO-1 knockdown (KD) MDCK monolayers. Here, we show that excessive contraction of subapical, but not perijunctional, actomyosin is responsible for the structural abnormalities induced by

This work was supported by NIDDK, National Institutes of Health (NIH), Grants F30DK103511 (to M. A. O.) and R01DK61931 and R01DK68271 (to J. R. T.) and NICHD, NIH, Grant T32HD007009 (to M. A. O.). The authors declare that they have no conflicts of interest with the contents of this article. The content is solely the responsibility of the authors and does not necessarily represent the official views of the National Institutes of Health.
This article was selected as one of our Editors' Picks.
This article contains Table S1, Figs. S1–S3, and Videos S1 and S2.
[1] To whom correspondence should be addressed: Brigham and Women's Hospital, Harvard Medical School, 77 Ave. Louis Pasteur, BHNRB 730, Boston, MA 02115. Tel.: 617-525-8165; E-mail: jrturner@bwh.harvard.edu.

[2] The abbreviations used are: ZO-1, zonula occludens-1; ZO-2, zonula occludens-2; ABR, actin-binding region; KD, knockdown; KO, knockout; latA, latrunculin A; LDMEM, low glucose (1 g/liter) Dulbecco's modified Eagle's medium; MDCK, Madin–Darby canine kidney; SEM, scanning electron microscopy; TEM, transmission electron microscopy; 3D, three-dimensional; BDM, butanedione monoxime; aa, amino acids; EGFP, enhanced GFP; PFA, paraformaldehyde; ANOVA, analysis of variance.

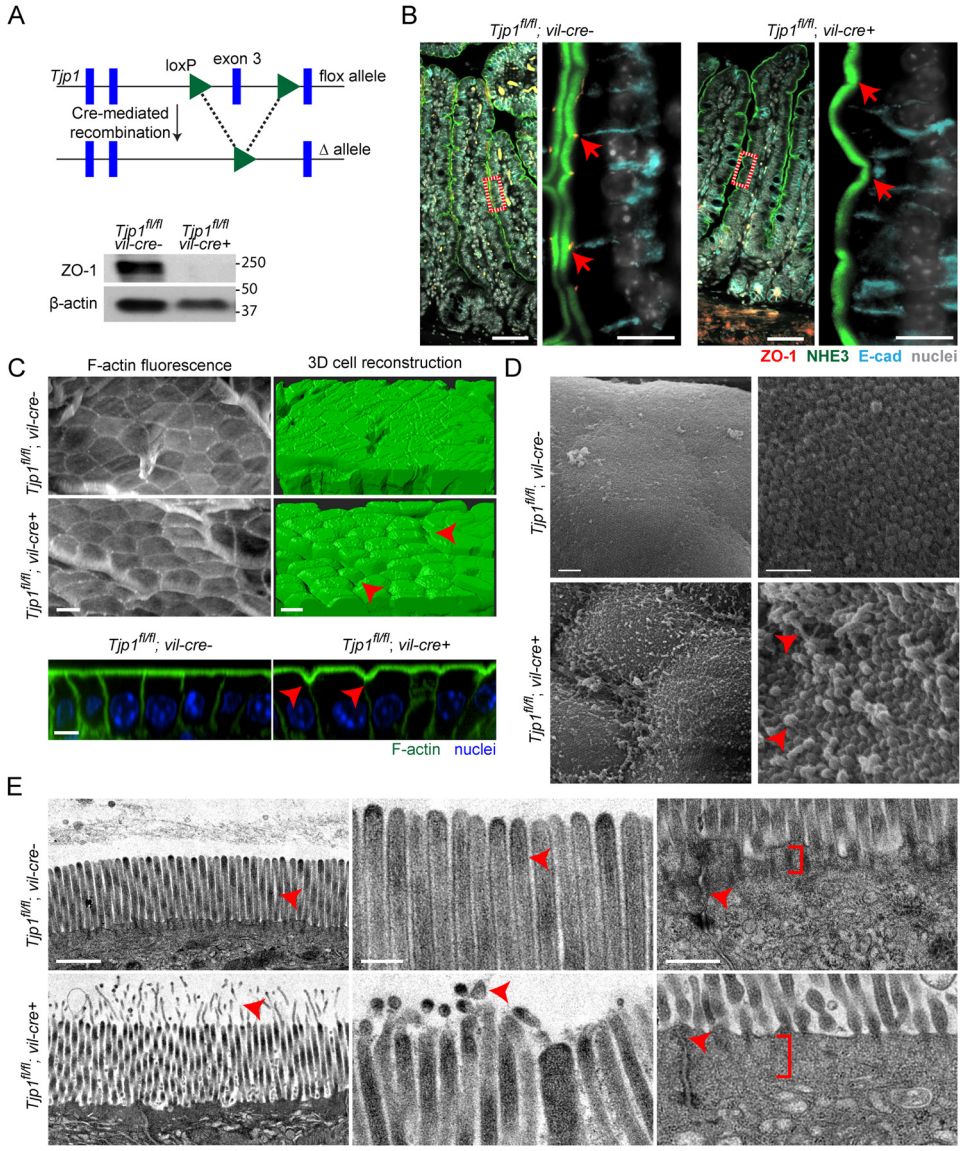

Figure 1. ZO-1 KO profoundly disrupts apical brush border structure of intestinal epithelia *in vivo*. *A*, schematic of Cre-mediated exon 3 deletion from the floxed *Tjp1* (ZO-1) allele. Intestinal epithelial cells from jejunum of WT (*Tjp1*$^{fl/fl}$; *vil-cre*$^{-}$) and intestinal epithelial-specific ZO-1 KO (*Tjp1*$^{fl/fl}$; *vil-cre*$^{+}$) mice were immunoblotted for ZO-1 and β-actin (as a loading control). *B*, photomicrographs of small intestine stained for the apical Na^+-H^+ exchanger NHE3 (*green*), ZO-1 (*red*), E-cadherin (*cyan*), and nuclei (Hoechst; *white*). *Boxes* in low-magnification images (*left*) indicate the regions shown at higher magnification (*right*). *Arrows* indicate sites of apical surface disruption in ZO-1 KO epithelium and intercellular junctions in both WT and ZO-1 KO epithelium. *Bars*, 100 μm (low magnification) and 10 μm (high magnification). *C*, 3D projections of F-actin (phalloidin) staining within the epithelium of small intestinal whole mounts from WT (*top*) and ZO-1 KO (*bottom*) mice (*left panels*) and 3D cellular reconstructions of the same images (*right panels*). *Bottom panels*, *x*,*z* projections from the same whole-mount images. *Arrowheads*, surface irregularities in ZO-1 KO epithelium. *Bars*, 5 μm. *D*, representative scanning electron micrographs of WT (*top*) and ZO-1 KO (*bottom*) jejunal epithelium. *Arrowheads*, irregular microvilli in ZO-1 KO epithelium. *Bars*, 1 μm (*left*) and 0.5 μm (*right*). *E*, representative transmission electron micrographs of WT (*top*) and ZO-1 KO (*bottom*) jejunal epithelium. *Arrowheads*, irregular microvillus structures (*left* and *middle*) and morphologically intact tight junctions (*right*). *Brackets* outline electron-dense terminal web. *Bars*, 1 μm (*left*), 0.3 μm (*middle*), and 0.5 μm (*right*).

ZO-1 deficiency, both *in vivo* and *in vitro*. Interactions mediated by the ZO-1 U5 and GuK domains are critical to actomyosin organization. ZO-1 lacking the PDZ1 domain can restore apical structure in ZO-2–sufficient, but not ZO-2–deficient, monolayers. This suggests that heterodimerization with ZO-2 can restore PDZ1-dependent ZO-1 functions. We conclude that ZO-1–mediated interactions within the apical junctional complex signal to apical F-actin to maintain uniform apical surfaces and that loss of these signals results in marked deformation of apical membranes and actin-based structures.

Results

In vivo ZO-1 knockout disrupts apical cell structure and apical tissue architecture

The obligate role of ZO-1 during embryogenesis (20) has limited *in vivo* study of ZO-1 to date. To overcome this obstacle, we generated intestinal epithelial cell–specific ZO-1 knockout (*Tjp1*$^{fl/fl}$; *villin-cre*$^{+}$) mice (Fig. 1*A*). These mice grew and reproduced normally with expected Mendelian ratios and were free of spontaneous disease under specific pathogen-free conditions. Western blotting of purified intestinal epithelia and

immunostains of intestinal tissue sections confirmed the absence of ZO-1 expression (Fig. 1, *A* and *B*). Crypt–villus architecture was maintained (Fig. 1*B*), but apical surface continuity was markedly disrupted. This included undulation of the apical surface brush border membrane and distinct crevasses at intercellular junctions between ZO-1 KO enterocytes.

To better define the altered apical morphology of ZO-1–deficient enterocytes, intact portions of jejunum were fixed and imaged without physical sectioning. Confocal slices of these phalloidin-stained tissues followed by 3D reconstruction showed distinct convex surfaces, with depressed intercellular junctions in ZO-1 KO, but not WT, epithelium (Fig. 1*C* and Video S1). These alterations were even more striking when viewed by scanning EM (SEM), where intercellular junctions between ZO-1–deficient enterocytes appeared as deep crevasses (Fig. 1*D*). In contrast, although the sites of intercellular junctions could be identified in WT enterocytes, they were subtle and were not depressed beneath the apical surface. SEM also revealed that the apical surface of ZO-1 KO epithelia appeared rough in contrast to the velvet-like brush border surfaces of WT epithelia (Fig. 1*D*). Higher magnification showed that the irregular apical surface of ZO-1 KO epithelia was due to highly variable microvillus length and diameter (Fig. 1*D*), in stark contrast to the regular length and uniform packing of microvilli in WT enterocytes.

Transmission EM (TEM) confirmed abnormal microvillus organization in ZO-1 KO epithelia (Fig. 1*E*). Long, nonparallel, thin strands extended beyond the normally uniform microvillus length and frequently included vesicles that were adherent to microvillus tips. Unlike the uniformly distributed and nearly identical-appearing microvillus rootlets seen at regular intervals in WT enterocytes (Fig. 1*E*), rootlet morphology and spacing were irregular in ZO-1 KO epithelia. Finally, ZO-1 KO intestinal epithelia included an expanded electron-dense zone beneath the apical membrane that obscured microvillus rootlets and excluded organelles (Fig. 1*E*, *brackets*). Conversely, tight junction structure was intact (Fig. 1*E*, *right panels*, *arrowheads*). Thus, despite displaying normal growth, reproduction, and overall tissue architecture, intestinal epithelial ZO-1 KO results in striking morphologic abnormalities that include disruption of apical surface architecture and microvilli with normal-appearing tight junctions.

ZO-1 knockdown in vitro phenocopies knockout in vivo

To determine whether *in vitro* ZO-1 KD recapitulates the striking *in vivo* effects of ZO-1 KO, WT (T23) and ZO-1 KD Madin–Darby canine kidney (MDCK) II cells were cultured to maturation on semipermeable supports, and apical structure was assessed by SEM and fluorescence microscopy (Fig. 2). As expected, WT monolayers displayed intact apical surfaces that were smooth and uniform. In contrast, apical surfaces of ZO-1 KD monolayers were disrupted by bulbous distensions. As a result, individual cell profiles were emphasized (Fig. 2*A*, *top panels*, *arrowheads*). Although less well-organized than intestinal epithelial brush borders, microvilli of WT MDCK monolayers were of uniform length. In contrast, ZO-1–deficient MDCK monolayers displayed microvilli with highly variable lengths (Fig. 2*A*, *bottom panels*, *arrowheads*), similar to ZO-1 KO enterocytes. ZO-2 KD monolayers were indistinguishable from WT, but apical surface and microvillus morphology of ZO-1/ZO-2 double-KD was markedly disrupted (Fig. 2). ZO-1, but not ZO-2, KD *in vitro* therefore causes disruptions of apical brush border membrane architecture similar to those induced by KO *in vivo*. In addition to demonstrating that the contributions of ZO-1 to apical architecture are generalizable beyond intestinal epithelium, these data indicate the dominant role of ZO-1, relative to ZO-2, in maintaining apical structure.

Apicobasal polarization is maintained in monolayers with irregular apical surfaces

Biogenesis of apical membranes is precisely controlled and is an essential component of epithelial polarization and brush border organization (18, 21–25). We therefore hypothesized that the striking morphological disruption of ZO-1–deficient cells might be accompanied by apicobasal polarity defects. Monolayers were stained for the apical marker podocalyxin/gp135, the apical polarity protein aPKCζ, and the basolateral adherens junction protein E-cadherin. Despite the abnormalities induced by ZO-1 KD, all lines formed confluent monolayers with correct apical–basal polarization (Fig. 2, *B* and *C*). This is consistent with the retained polarized distributions of NHE3 and E-cadherin *in vivo* (Fig. 1*B*).

Changes in cell shape are frequently secondary to alterations in actomyosin organization and contractility (4, 26). Consistent with this, both *x*,*z* reconstructions and 3D surface reconstructions of the dome-like apical surface deformations revealed dense accumulations of F-actin just below the apical membranes of ZO-1 KD epithelia (Fig. 2 (*C* and *D*) and Video S2). This F-actin organization is seen in *x*,*y* projections as dense cytoplasmic F-actin rings (Fig. 2*B*, *arrowheads*). These were not seen in WT and ZO-2 KD monolayers but were only present in ZO-1 KD and ZO-1/ZO-2 double-KD monolayers. We thus considered the possibility that the F-actin rings were a consequence of increased actomyosin contractility. Increases in actomyosin contraction have been reported in ZO-1/ZO-2 double-KD cells but were associated with perijunctional F-actin and myosin IIB intensification and reorganization into a sarcomere-like banded pattern (26, 27). This perijunctional F-actin and myosin IIB reorganization was not present in ZO-1 KD monolayers. However, ZO-1 KD showed clear myosin IIB rings that coincided with the F-actin rings (Fig. 2*B*, *zoomed panels*). These were also present in ZO-1/ZO-2 double-KD cells, but were distributed over larger areas, consistent with the more severe phenotype of these cells. These data suggest that ZO-2 can partially compensate for ZO-1 deficiency in terms of perijunctional actomyosin organization. Nevertheless, ZO-1 deficiency alone is sufficient to induce dense, cytoplasmic F-actin rings that are separate from perijunctional F-actin. To avoid confounding results related to the additional changes induced by ZO-1/ZO-2 double-KD, our studies of ZO protein function and regulation of apical structure therefore focused on ZO-1 single-KD monolayers and tissues.

In addition to corroborating the SEM results, orthogonal *x*,*z* projections also demonstrated that the apical distensions induced by ZO-1 depletion were enriched in gp135, aPKCζ, and

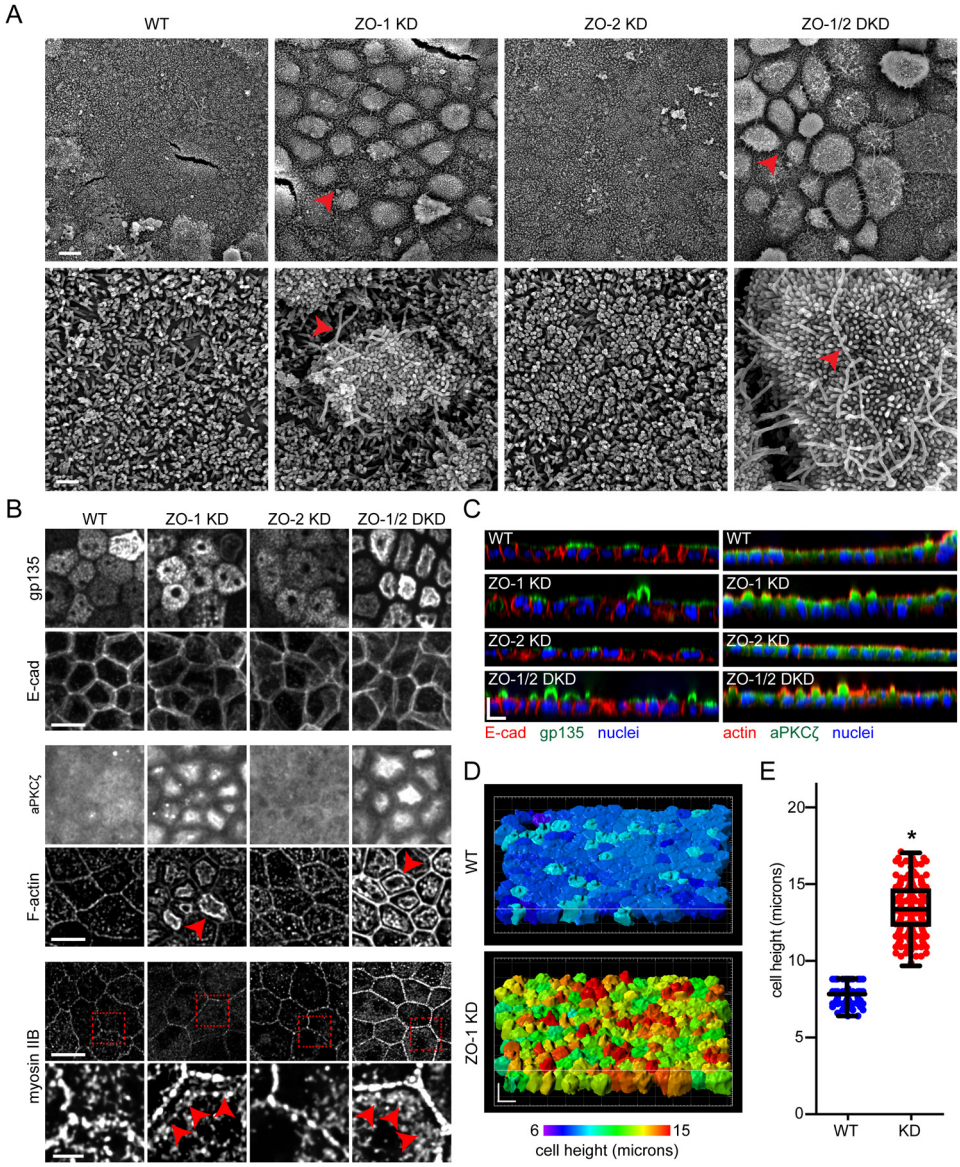

Figure 2. *In vitro* ZO-1, but not ZO-2, KD recapitulates the aberrant apical architecture induced by ZO-1 KO *in vivo*. *A*, representative low-magnification (*top*) and high-magnification (*bottom*) SEM images from confluent WT, ZO-1KD, ZO-2 KD, and ZO-1/ZO-2 double-KD monolayers. *Arrowheads*, intercellular junctions (low magnification) and abnormal microvilli (high magnification). *Bars*, 5 μm (*top panels*) and 1 μm (*bottom panels*). *B*, confluent monolayers were immunostained for podocalyxin/gp135 and E-cadherin, aPKCζ and F-actin (phalloidin), or myosin IIB. F-actin, aPKCζ, gp135, and E-cadherin images are maximum projections of the full monolayer thickness. Myosin IIB images are of a single confocal *z*-slice; *zoomed views* of the *boxed areas* are shown *below* each image. All low magnification images for each antigen are scaled identically; the high-power views of myosin-IIB are scaled individually to demonstrate the rings that colocalize with F-actin. *Arrowheads*, prominent cytoplasmic (subapical) F-actin and myosin-IIB rings in ZO-1 KD and ZO-1/ZO-2 double-KD monolayers. *Bars*, 10 μm and 30 μm for *zoomed images*. *C*, projections (*x*,*z*) of confluent monolayers stained for gp135 (*green*), E-cadherin (*red*), and nuclei (Hoechst; *blue*) (*left panels*) or F-actin (phalloidin; *red*), aPKCζ (*green*), and nuclei (Hoechst; *blue*) (*right panels*). *Bars*, 10 μm. *D*, confluent WT and ZO-1 KD monolayers subjected to calcium switch were fixed and stained for F-actin (phalloidin) 24 h after calcium repletion. 3D reconstructions of confocal *z*-stacks of F-actin images were created, and cell reconstructions are *color-coded* by height as indicated. *Bar*, 10 μm. *E*, graphical representation of cell height quantification. *Boxes* enclose second and third quartiles, the *center bar* indicates the mean, and *bars* extend to maximum and minimum values. Data shown are from one experiment representative of three independent studies *, $p < 0.001$ by two-tailed *t* test comparing WT ($n = 198$) with KD ($n = 188$).

F-actin (Fig. 2*C*). Thus, ZO-1 KD has little effect on perijunctional actomyosin but induces striking changes in subapical F-actin and microvillus structure. To better define the altered morphology of ZO-1–deficient monolayers, 3D reconstructions of F-actin distribution within each cell were created, and the height of each cell was measured (Fig. 2*D*). ZO-1 KD cells were taller and had markedly greater cell height variation than WT cells ($p < 0.0001$) (Fig. 2*E*).

We and others have shown that ZO-1 regulates epithelial proliferation *in vitro* (18, 28, 29). We therefore considered the possibility that increased crowding of ZO-1 KD monolayers was responsible for the apical distensions. One could, for example, hypothesize that, to maintain cell volume, cells became thinner and more elongated as proliferation continued in ZO-1 KD monolayers. However, the basolateral cross-sectional area of ZO-1 KD and WT cells in mature monolayers was similar (WT, 157.1 ± 35.2 μm^2 ($n = 137$); KD, 150.4 ± 35.2 μm^2 ($n = 152$); $p = 0.12$ by two-tailed *t* test). Further, calcium-switch assays showed that WT and ZO-1 KD monolayers reached steady-state barrier function with similar kinetics (Fig. S1*A*).

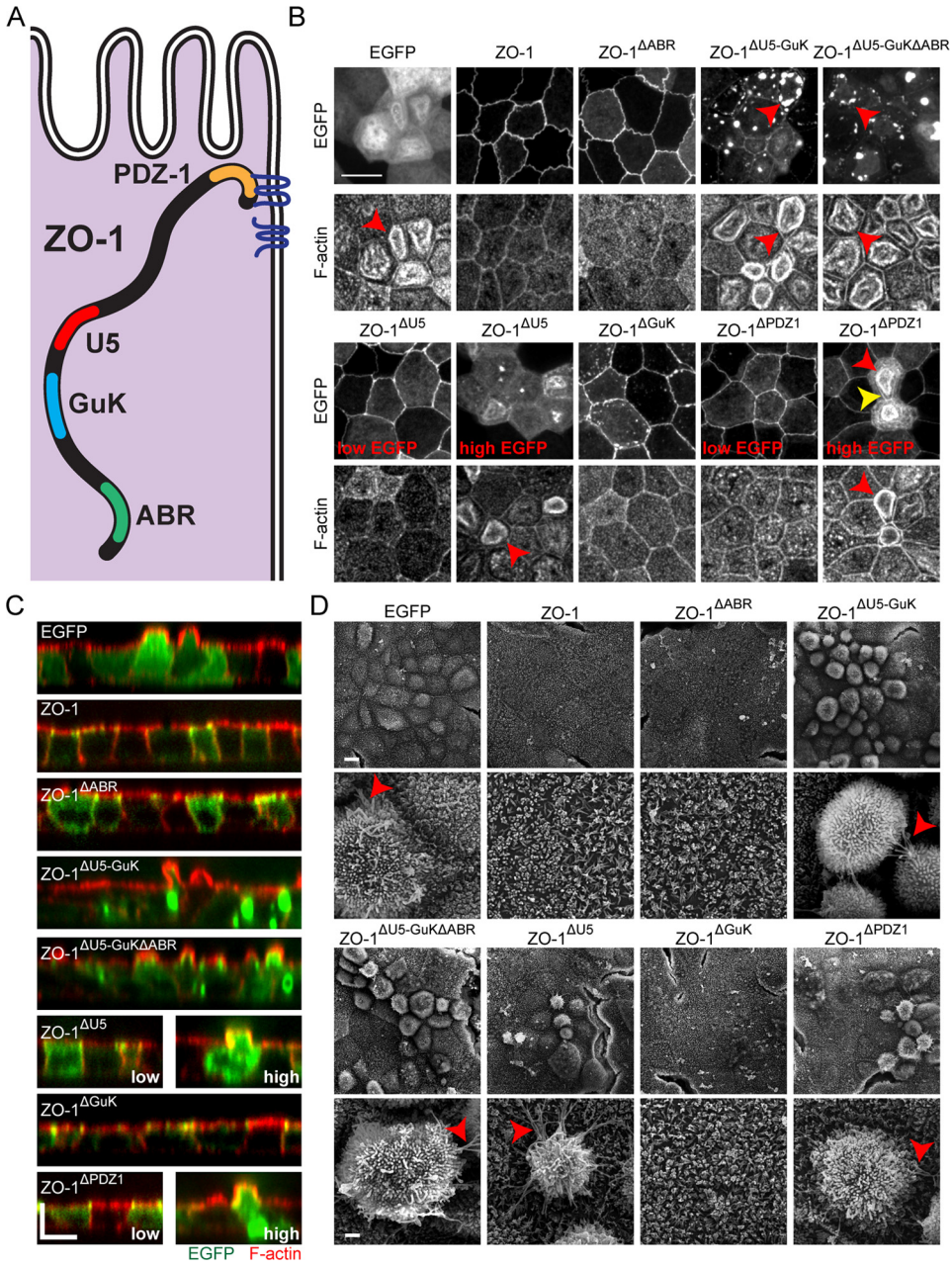

Figure 3. Multiple ZO-1 structural domains orchestrate F-actin, apical cell structure, and microvillus organization. *A*, diagram depicting ZO-1 structural domains and PDZ1 domain interactions with the C terminus of claudin proteins. *B*, confluent ZO-1 KD monolayers expressing the indicated EGFP-tagged ZO-1 mutant protein were subjected to calcium switch, stained for F-actin (phalloidin) 24 h after calcium repletion, and imaged with confocal *z*-stacks. Representative images of EGFP proteins are maximal projections of a 7-μm section beginning at the apical surface. For F-actin, full-monolayer thickness maximal projections are shown. *Red arrowheads*, cytoplasmic F-actin rings and corresponding EGFP localization. *Yellow arrowhead*, recruitment of the EGFP-tagged ZO-1$^{\Delta PDZ1}$ to the tight junction in a high-expressing cell. All F-actin images are scaled identically. Due to heterogeneity of EGFP expression, EGFP images are scaled independently. *Bar*, 10 μm. *C*, representative *x*,*z* projections of ZO-1 KD monolayers expressing the indicated EGFP-tagged ZO-1 mutant protein (*green*) and stained for F-actin (phalloidin; *red*). *Bar*, 10 μm. *D*, SEM images of confluent ZO-1 KD MDCK monolayers expressing the indicated ZO-1 mutant protein. Lower magnification images (*top panels*) depict overall apical surface architecture, and higher magnification images (*bottom panels*) show more detailed views of apical cell structure and microvillus organization. *Arrowheads*, aberrant microvillus organization associated with apical surface distensions. *Bars*, 5 μm (*top panels*) and 1 μm (*bottom panels*).

Nevertheless, even during this rapid barrier development, ZO-1 KD cells displayed cytoplasmic F-actin rings when viewed in *x*,*y* projections and the corresponding apical distensions seen in *x*,*z* reconstructions (Fig. S1, *B* and *C*). Together, these data indicate that ZO-1, but not ZO-2, regulates apical membrane morphology and cortical F-actin structure *in vivo* and *in vitro*.

ZO-1 structural domains coordinate apical surface development

ZO-1 is a scaffolding protein with multiple structural domains (Fig. 3*A*) that coordinate binding partners to regulate tight junction and adherens junction protein recruitment and assembly, perijunctional F-actin organization, and epithelial morphogenesis (18, 30–33). We tested the hypothesis that spe-

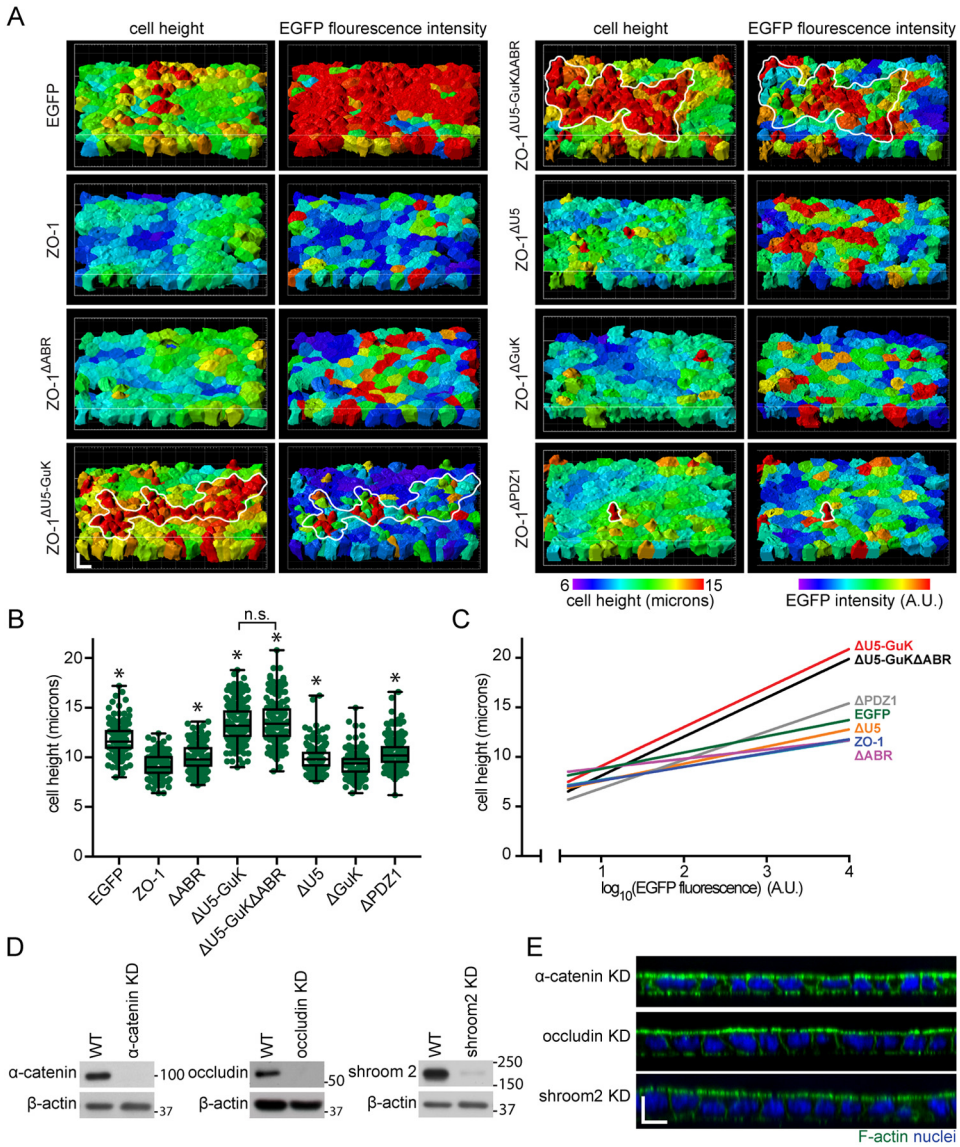

Figure 4. ZO-1 structural domains determine cell height and apical surface architecture. *A*, confluent ZO-1 KD monolayers expressing the indicated EGFP-tagged ZO-1 mutant protein were subjected to calcium switch and stained for F-actin 24 h after calcium repletion. 3D renderings of individual cells were created using F-actin as a membrane marker. Cells are *colored* by height (*left panels*) and EGFP fluorescence intensity (*right panels*), as indicated. *White lines* outline areas expressing relatively high levels of EGFP-tagged mutants. *Bar*, 10 μm. *B*, height of each 3D cell is shown. *Boxes* enclose second and third quartiles, the *center bar* indicates the mean, and *bars* extend to maximum and minimum values. Data shown are from one experiment that is representative of three independent studies. *, $p < 0.001$; *n.s.*, $p > 0.05$ by one-way ANOVA with Kruskal–Wallis post-test comparing the indicated cell line with the full-length ZO-1–expressing cell line. $n = 170$ (EGFP), 145 (ZO-1), 145 (ZO-1$^{\Delta ABR}$), 187 (ZO-1$^{\Delta U5\text{-}GuK}$), 147 (ZO-1 $^{\Delta U5\text{-}GuK\Delta ABR}$), 160 (ZO-1$^{\Delta U5}$), and 172 (ZO-1$^{\Delta PDZ1}$). *C*, cell height plotted as a function of $\log_{10}$(EGFP fluorescence). A line of best fit was generated for each ZO-1 transgene. *D*, stable KD of α-catenin, occludin, or shroom2 was confirmed by Western blotting. *E*, *x,z* projections of confluent α-catenin, occludin, or shroom2 KD monolayers stained for F-actin (phalloidin, *green*) and nuclei (Hoescht, *blue*). *Bar*, 10 μm.

cific ZO-1 structural domains mediate development of a uniform apical surface by expressing EGFP-tagged ZO-1 mutants in the ZO-1 KD cell line (Fig. 3*A* and Fig. S2). Expression of free EGFP had no effect on apical F-actin accumulation or membrane distensions, but EGFP-tagged full-length ZO-1 localized to normal-appearing tight junctions and restored both F-actin organization and a uniform apical surface (Fig. 3, *B* and *C*). This was confirmed by SEM, which demonstrated restoration of normal microvillus brush border structure (Fig. 3*D*). Uniform apical surface restoration was characterized by shorter cells with less variation in cell height (Fig. 4, *A* and *B*; $p < 0.0001$). In addition to demonstrating that EGFP-tagged ZO-1 is functional, these data show that the observed phenotype is specific to ZO-1 loss.

Given striking differences in F-actin organization upon ZO-1 loss, we next tested whether the actin-binding region (ABR) is required for ZO-1–dependent F-actin organization. Expression of EGFP-tagged ZO-1$^{\Delta ABR}$ in ZO-1 KD cells restored morphology in a manner similar to full-length ZO-1 (Fig. 3, *B* and *C*). Specifically, ZO-1$^{\Delta ABR}$ localized to normal-appearing tight junctions (Fig. 3*B*), restored both uniform apical surfaces and microvillus architecture (Fig. 3, *C* and *D*), and decreased cell height (Fig. 4, *A* and *B*; $p < 0.001$). Whereas cell height of ZO-1$^{\Delta ABR}$–expressing cells was statistically greater than that of

cells expressing full-length ZO-1 (Fig. 4*B*), the absolute difference was small (9.2 ± 1.2 μm *versus* 10.1 ± 1.4 μm), and restoration of a uniform apical surface was accompanied by a reduction in cell height variance. This indicates that the ZO-1 ABR is dispensable for both F-actin and apical surface organization.

The U5-GuK region within the N terminus of ZO-1 has been reported to regulate perijunctional actomyosin structure (30, 33). In ZO-1 KD cells, EGFP-tagged ZO-1$^{\Delta U5\text{-}GuK}$ localized to tight junctions but was more prominent within cytoplasmic punctae (Fig. 3, *B* and *C*). Fluorescence microscopy showed that ZO-1$^{\Delta U5\text{-}GuK}$ failed to eliminate cytoplasmic F-actin rings, as seen in *x*,*y* projections, and actually enhanced the density of these rings (Fig. 3*B*). Consistent with this, SEM showed that apical distensions increased in prominence in monolayers expressing ZO-1$^{\Delta U5\text{-}GuK}$ relative to those expressing free EGFP alone (Fig. 3*D*). Further, ZO-1$^{\Delta U5\text{-}GuK}$ expression increased both average cell height and cell height variation (Fig. 4, *A* and *B*; $p < 0.001$). In addition to cell height, the EGFP fluorescence intensity of ZO-1$^{\Delta U5\text{-}GuK}$–expressing cells varied significantly throughout the monolayers (Fig. 4*A*). Direct comparisons show a direct correlation between increased EGFP fluorescence intensity and increased cell height (Fig. 4, *A* and *C*). These data suggest that, not only did ZO-1$^{\Delta U5\text{-}GuK}$ fail to restore cortical F-actin and apical tissue architecture, but it exacerbated the defect induced by ZO-1 KD.

We considered the hypothesis that ZO-1$^{\Delta U5\text{-}GuK}$ could be acting as a dominant-negative effector of F-actin organization, given that it was likely to bind F-actin but unable to interact with U5-GuK binding partners. This could explain the correlation between increased expression and increased cell height in ZO-1$^{\Delta U5\text{-}GuK}$-transfected monolayers. We therefore assessed the impact of expressing ZO-1 lacking both the U5-GuK and ABR domains (EGFP-tagged ZO-1$^{\Delta U5\text{-}GuK\Delta ABR}$). This construct behaved identically to the ZO-1$^{\Delta U5\text{-}GuK}$ construct by increasing cell height in an expression-dependent manner (Figs. 3 and 4). These observations confirm the conclusion above that the ABR is unnecessary for uniform apical surface formation in a ZO-1–deficient background and, more importantly, indicate that the U5-GuK region of ZO-1 is central to organization of apical F-actin and apical cell structure. One possible explanation for this could be defective recruitment of known U5-GuK binding partners to the apical junctional complex. However, stable KD of each of the three proteins known to bind the U5-GuK domain, occludin, shroom2, and α-catenin (18, 34–37), had no effect on F-actin organization or apical surface structure (Fig. 4, *D* and *E*).

Based on the striking phenotype induced by deletion of U5 and GuK domains and reported functional differences between these regions (33), we expressed ZO-1$^{\Delta U5}$ and ZO-1$^{\Delta GuK}$ in ZO-1 KD cells. In cells with lower levels of ZO-1$^{\Delta U5}$ expression, the protein was recruited to tight junctions and rescued morphology of ZO-1 KD epithelia (Figs. 3 and 4). In cells with higher levels of expression, ZO-1$^{\Delta U5}$ was distributed diffusely throughout the cytoplasm and within cytoplasmic punctae (Fig. 3, *B* and *C*). These cells stood out due to their dense F-actin rings and large apical distensions. Although we could not correlate morphology with individual cell transgene expression in SEM images, a similar fraction of cells were noted to have distended apical membranes, loss of microvillus architecture, and deep crevasses at intercellular junctions (Fig. 3*D*). In contrast, ZO-1$^{\Delta GuK}$ localized to the tight junction and restored cortical F-actin, microvillus architecture, cell height, and apical surface in a manner similar to full-length ZO-1 (Figs. 3 and 4).

Similar to ZO-1$^{\Delta U5}$, ZO-1$^{\Delta PDZ1}$ expression resulted in two distinct phenotypes. In cells with low levels of expression, ZO-1$^{\Delta PDZ1}$ largely rescued F-actin structure, microvillus architecture, and apical surface structure (Figs. 3 and 4). However, cells with higher levels of ZO-1$^{\Delta PDZ1}$ expression displayed dense accumulations of the transgene within apical distensions and apical F-actin rings (Figs. 3 and 4). Similar heterogeneity was apparent in SEM images, where many areas of the monolayer resumed a nearly normal morphology, but clusters of cells with apical distensions and abnormal microvilli persisted (Fig. 3*D*).

ZO-1$^{\Delta PDZ1}$ rescues epithelial architecture in a ZO-2–dependent manner

The data above highlight the unique functions of each of the tested ZO-1 structural domains. The results were, however, difficult to understand in some contexts. For example, why did deletion of U5-GuK domains exacerbate the phenotype of ZO-1 KD monolayers? One potential explanation for these data is that the U5-GuK deletion mutant acted as a dominant-negative protein that inhibited ZO-2 function. A dominant-negative function might also explain why constructs lacking U5 or PDZ1 domains displayed dose-dependent effects, with lower levels of expression restoring function and higher levels having detrimental effects. One could postulate that low-level expression allowed ZO-1/ZO-2 heterodimers to rescue function, whereas higher levels of ZO-1 favored formation of defective ZO-1 dimers that outcompeted ZO-1/ZO-2 heterodimers.

To investigate a potential compensatory role for ZO-2 structural domains in ZO-1 KD cells, EGFP-tagged ZO-1 mutants were expressed in ZO-1/ZO-2 double-KD cells. Monolayers expressing free EGFP displayed the expected cytoplasmic F-actin rings and apical distensions (Fig. 5, *A* and *B*). In contrast to ZO-1 single-KD monolayers, ZO-1$^{\Delta PDZ1}$ was unable to rescue F-actin organization or apical cell structure in ZO-1/ZO-2 double-KD monolayers, regardless of expression level. These data suggest that ZO-1$^{\Delta PDZ1}$ expression rescued ZO-1 single-KD monolayers by dimerizing with ZO-2 to create a fully functional heterodimer (Fig. 5*C*). The data further indicate that PDZ1-mediated interactions are essential to ZO-1–dependent organization of cortical F-actin and assembly of uniform apical surfaces.

As in ZO-1 single-KD cells, expression of either ZO-1$^{\Delta U5\text{-}GuK}$ or ZO-1$^{\Delta U5\text{-}GuK\Delta ABR}$ failed to rescue morphology (Fig. 5, *A* and *B*). However, unlike ZO-1 KD cells, expression of these mutants did not appear to exacerbate the phenotype of ZO-1/ZO-2 double-KD cells. As in ZO-1 single-KD cells, low levels of ZO-1$^{\Delta U5}$ expression partially restored F-actin structure and reduced the magnitude of apical distensions in ZO-1/ZO-2 double-KD cells. However, high levels of ZO-1$^{\Delta U5}$ expression also partially rescued and did not make the phenotype more severe (Fig. 5, *A* and *B*). These data support the hypothesis that the detrimental effect of high-level ZO-1$^{\Delta U5}$ expression in ZO-1 single-KD

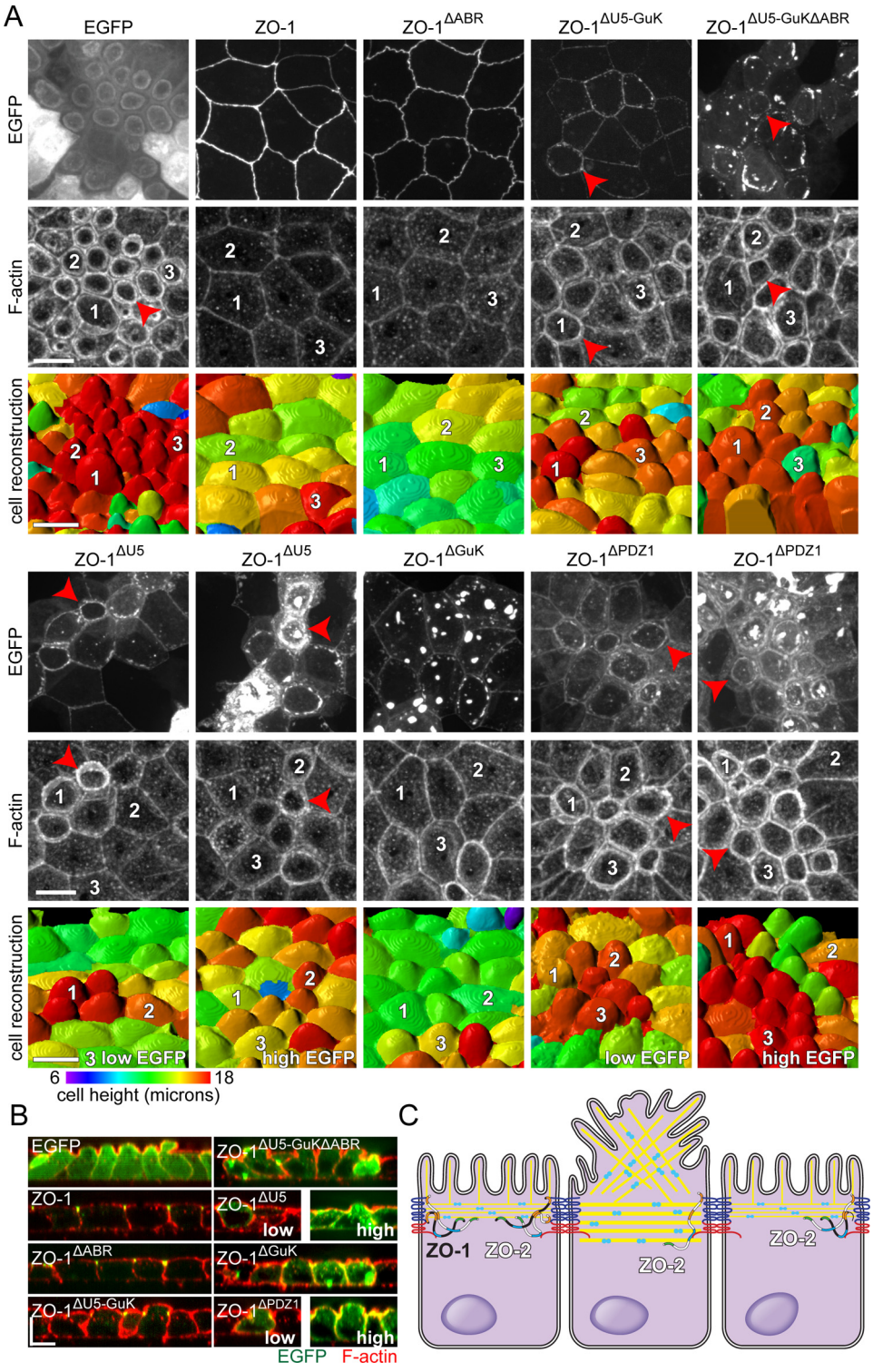

Figure 5. ZO-1 and ZO-2 heterodimers maintain uniform apical surfaces. *A*, confluent ZO-1/ZO-2 double-KD monolayers expressing the indicated EGFP-tagged ZO-1 mutant protein were subjected to calcium switch, stained for F-actin (phalloidin) 24 h post-calcium repletion, and imaged. Representative images of EGFP proteins are maximal projections of a 7-μm section that extends from the apical surface of the monolayer (*top*). Full-monolayer thickness maximal projections of F-actin staining are shown (*middle*). Cell reconstructions were created using F-actin as a membrane marker and coded by cell height as shown (*bottom*). Three cells in each F-actin image and corresponding 3D reconstruction are *numbered* for orientation. *Arrowheads*, cytoplasmic F-actin rings and corresponding EGFP localization at sites of apical distension. All F-actin images are scaled identically. Due to heterogeneity of expression, EGFP images are scaled independently. *Bar*, 10 μm. *B*, representative *x,z* projections of ZO-1/2 double-KD monolayers expressing the indicated EGFP-ZO-1 mutant protein (*green*) and stained for F-actin (phalloidin, *red*). *Bar*, 10 μm. *C*, model of ZO-1 and ZO-2 heterodimers rescuing regular apical surfaces. The *left cell* represents a WT cell, which expresses both ZO-1 and ZO-2 and has a uniform apical surface. The *center cell* represents a ZO-1 KD cell, which has a distended apical surface and accumulation of cortical F-actin. Finally, the *right cell* is a ZO-1 KD cell expressing a ZO-1 mutant lacking the PDZ1 domain. ZO-1$^{\Delta PDZ1}$ can rescue actin organization and promote uniform apical surface development in the presence of ZO-2, but not in ZO-1/ZO-2 double-KD cells, through ZO-1 mutant dimerization with ZO-2 and functional redundancy of some ZO-1 and ZO-2 structural domains.

monolayers was due to inhibition of ZO-2 function. These data also suggest that the U5 domain contributes to ZO-1–dependent organization of F-actin and apical membrane structures to only a minor degree.

Finally, expression of ZO-1, ZO-1$^{\Delta ABR}$, or ZO-1$^{\Delta GuK}$ in double-KD cells restored cortical F-actin and apical membrane structure. ZO-2, therefore, did not provide the ABR domain that allowed ZO-1$^{\Delta ABR}$ to rescue morphology. Thus, despite the profound F-actin disruption, ZO protein ABR domains are not required to restore normal apical structure.

ZO-1 directs uniform apical surface assembly by regulating actomyosin architecture

The dense cytoplasmic actomyosin that characterizes ZO-1 KO and KD epithelia suggests that hypercontractility of this cytoskeletal network may be responsible for the irregular apical surfaces that characterize these epithelia. To test this hypothesis, we screened the effect of pharmacologic agents that target different aspects of cytoskeletal function. In each case, a range of concentrations was tested. To minimize the duration of drug exposure, monolayers were grown to confluence and then cultured in low-calcium medium for 16 h to disrupt cell–cell junctions. Pharmacological agents were added at the time of calcium repletion, and monolayers were harvested after 24 h, at which time uniform apical surfaces are well-established in WT monolayers (Fig. S1).

To determine whether F-actin and apical membrane abnormalities of ZO-1 KD monolayers reflected aberrant microfilament function, monolayers were treated with latrunculin A (latA), which binds actin monomers and prevents their polymerization (38). In WT monolayers, latA disrupted F-actin in a dose-dependent manner. The lowest dose (0.05 μM) had no effect, but the intermediate dose (0.5 μM) profoundly disrupted cortical F-actin in WT monolayers and also interfered with delivery of gp135 to apical membranes (Fig. 6, *A* and *B*). In contrast, 0.5 μM latA selectively depleted cytoplasmic F-actin rings within ZO-1 KD monolayers without disrupting other F-actin structures (Fig. 6, *A* and *B*). gp135 delivery to uniform apical membranes was also restored by 0.5 μM latA. Morphometric analysis confirmed that 0.5 μM latA reduced both cell height and the variance of cell height in ZO-1 KD monolayers (Fig. 6, *C* and *D*; $p < 0.0001$). At the highest dose (1.5 μM), latA disrupted perijunctional and cortical F-actin in both WT and ZO-1 KD monolayers. latA reduced, but did not eliminate, the long, thin microvillus extensions induced by ZO-1 KD. latA also induced microvillus clustering in both the presence and absence of ZO-1. Thus, F-actin disruption partially corrected the microvillus phenotype of ZO-1 KD epithelium, suggesting that excessive actin polymerization contributes to the apical abnormalities observed.

Inhibition of F-actin polymerization has multiple effects. These include disruption of myosin II motor activity, which has been linked to epithelial cell shape, morphogenesis, tight junction barrier regulation, and ZO-1 exchange between tight junction and cytoplasmic pools (5, 17, 39–41). We therefore assessed the impact of myosin motor ATPase inhibitors on apical surface structures (Figs. 7 and 8) (42–47). Blebbistatin did not disrupt apical surfaces in WT cells but reduced the magnitude of apical distensions and the intensity of cytoplasmic F-actin rings in ZO-1 KD monolayers in a dose-dependent manner (Fig. 7, *A–C*). Morphometric analysis confirmed that, at the highest dose (100 μM), blebbistatin significantly reduced the height of ZO-1 KD epithelia (Fig. 7, *C* and *D*; $p < 0.0001$). However, blebbistatin also reduced the height of WT epithelia (Fig. 7, *C* and *D*; $p < 0.0001$) and, paradoxically, induced straightening of perijunctional F-actin profiles at all three doses tested in WT monolayers (Fig. 7, *A–C*). Blebbistatin fully eliminated the bizarre microvillus extensions that characterized ZO-1 KD epithelia. Thus, whereas blebbistatin-mediated myosin motor inhibition did improve the ZO-1 KD phenotype, rescue was only partial.

A second myosin motor inhibitor, 2,3-butanedione monoxime (BDM), is used infrequently due to numerous reports of off-target effects, primarily in muscle cells (47, 48). Nevertheless, it is structurally unrelated to blebbistatin and unlikely to have shared off-target effects despite also inhibiting myosin II activity. In WT monolayers, BDM had no observable effect on F-actin organization or assembly of uniform apical surfaces but did cause a dose-dependent decrease in apical gp135 delivery (Fig. 8, *A* and *B*). When ZO-1 KD monolayers were treated with BDM, cytoplasmic F-actin rings were eliminated, and normal apical surface architecture was reestablished in a dose-dependent manner (Fig. 8). As in WT cells, BDM reduced the intensity of gp135 staining at the apical membranes of ZO-1 KD monolayers (Fig. 8, *A* and *B*). BDM also reduced the height of both WT and ZO-1 KD monolayers. As a result, ZO-1 KD monolayers treated with the highest dose of BDM (10 mM) had indistinguishable morphology and statistically identical heights to WT monolayers treated with low-dose BDM (1 mM) (Fig. 8, *C* and *D*). Rescue by BDM included normalization of microvillus architecture.

We considered potential off-target effects of BMD. The most likely off-target effect in epithelial cells is inhibition of Ca^{2+}-dependent myosin light-chain kinase activation. However, a highly specific myosin light chain kinase inhibitor, PIK (49, 50), had no effect on apical structure of WT or ZO-1 KD monolayers (data not shown). Notably, relative to blebbistatin, BDM resulted in greater restoration of normal apical morphology, including microvillus structure. This could be interpreted as reflecting off-target effects of BDM or incomplete myosin motor inhibition by blebbistatin. Nevertheless, the overlapping effects of blebbistatin and BDM indicate that myosin motor activity is a significant contributor to the dense cytoplasmic F-actin rings, apical distensions, and abnormal microvilli seen in ZO-1 KD cells.

In contrast to myosin motor inhibitors, pharmacological agents targeting Cdc42 (ML141) and Rho kinase (Y27632) were unable to rescue apical structure in ZO-1 KD monolayers (51, 52). Cdc42 inhibition had no effect on WT monolayers, but treatment with an intermediate dose (10 μM) increased both the proportion of ZO-1 KD cells with apical distensions and cell height (Fig. S3; $p < 0.001$). Rho kinase inhibition had no effect on cell height but induced aberrant polarization (Fig. S4). Abnormalities included stacked nuclei as well as F-actin– and gp135–positive membrane structures at cell–cell contacts and cell rounding at the highest dose. These changes were present in WT and ZO-1 KD monolayers and were therefore independent of ZO-1 expression.

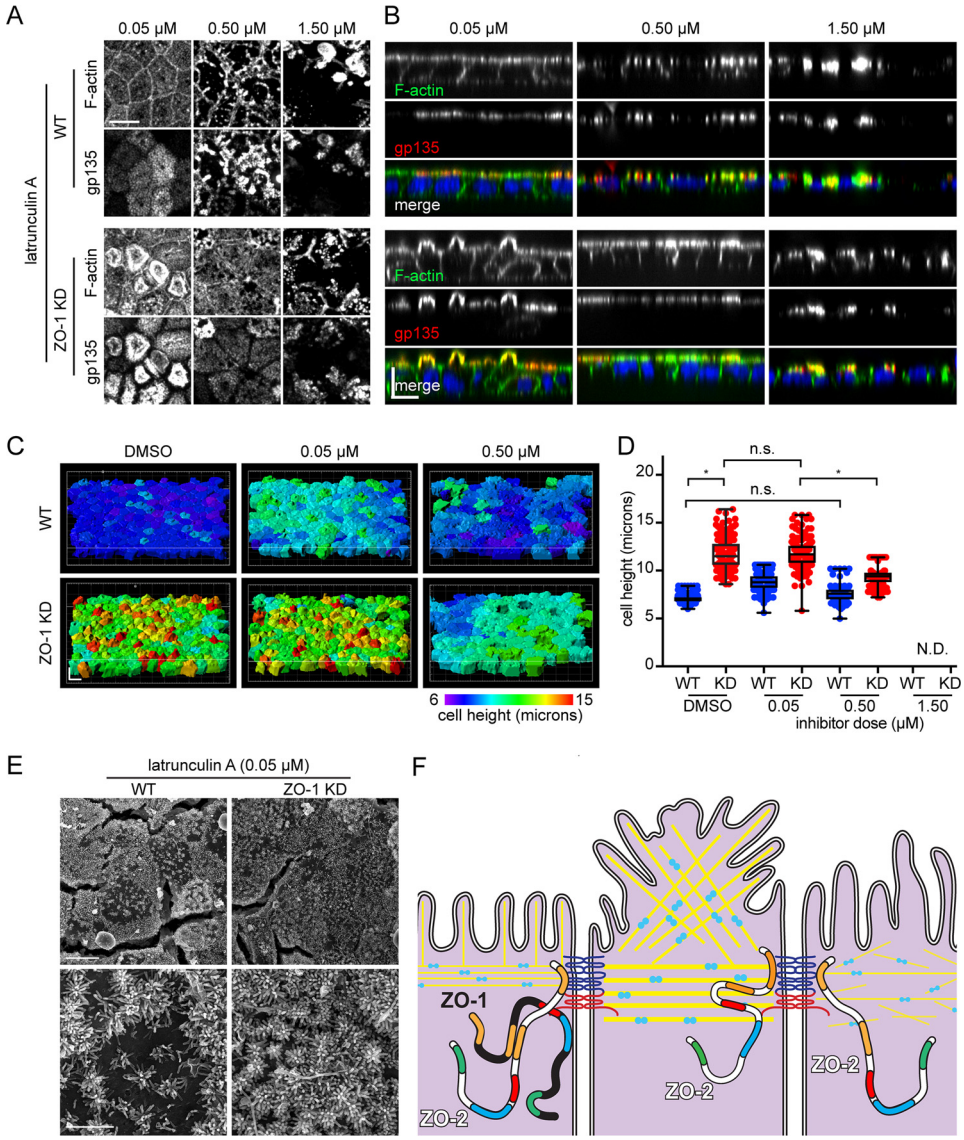

Figure 6. Actin microfilaments are necessary for apical surface distension in ZO-1 KD monolayers. *A* and *B*, confluent WT and ZO-1 KD monolayers were subjected to calcium switch and treated with 0.05, 0.50, or 1.50 μM latrunculin A upon calcium repletion. Monolayers were stained for F-actin (phalloidin; *green*), podocalyxin/gp135 (*red*), and nuclei (Hoechst; *blue*). Representative maximal projections of full-monolayer thickness *z*-stacks and *x*,*z* projections are shown. All images for a given antigen and image orientation are scaled identically. *Bars*, 10 μm. *C*, 3D renderings of individual cells were generated using F-actin as a membrane marker. Renderings could not be created at the highest dose of latrunculin A (1.5 μM) due to marked F-actin disruption. Cells are *colored* based on cell height, as indicated. *Bar*, 10 μM. *D*, height of each 3D cell rendering was determined. *Box*, second and third quartile; *central bar*, mean; *bars* extend to maximum and minimum values. Data are from one experiment representative of three independent studies. For WT, $n = 191$, 158, and 98 for vehicle, 0.05 μM, and 0.50 μM, respectively; for KD, $n = 178$, 170, and 111 for vehicle, 0.05 μM, and 0.50 μM, respectively. *n.s.*, $p > 0.05$; *, $p < 0.001$ by one-way ANOVA with Kruskal–Wallis post-test for comparison indicated by *brackets*. *E*, scanning electron micrographs of WT and ZO-1 KD monolayers treated with latrunculin A for 24 h after calcium switch. *Bar*, 10 μm (*top*) and 3 μm (*bottom*). *F*, diagram depicting regular apical surface in a WT cell (*left*), abnormal F-actin accumulation and apical distension in a ZO-1 KD cell (*middle*), and restoration of normal apical architecture upon pharmacologic disruption of F-actin in a ZO-1 KD cell (*right*).

Dynamin inhibition corrects apical surface expansion

Myosin motors and actin have been linked to endocytosis and exocytosis (53–60). We therefore considered the possibility that either excessive delivery of membrane to the apical surface or defective endocytic or exocytic removal contributed to the apical expansion observed. To test this hypothesis, we asked whether inhibition of dynamin II, an effector GTPase that mediates membrane fission, modified the phenotype of ZO-1 KD epithelia. Dynamin inhibition in ZO-1 KD monolayers resulted in flattening of the apical surface into a normal architecture, eliminated F-actin rings, and partially normalized microvillus architecture (Fig. 9). These data suggest that disruption of normal membrane traffic contributes to the expanded apical surface of ZO-1–deficient epithelial cells. These data, however, must be interpreted cautiously, as the inhibitor used, dynasore (61), has been criticized as nonspecific because it also interferes with membrane ruffling and destabilizes F-actin, even in cells lacking all three dynamins (62). Nonetheless, expression of defective dynamin II mutants in epithelial cells has demonstrated a role for dynamin in regulating actomyosin cytoskeletal structure and epithelial polarization (54). This may explain why newer dynamin inhibitors thought to have greater specificity also inhibit membrane ruffling and destabilize F-actin (62).

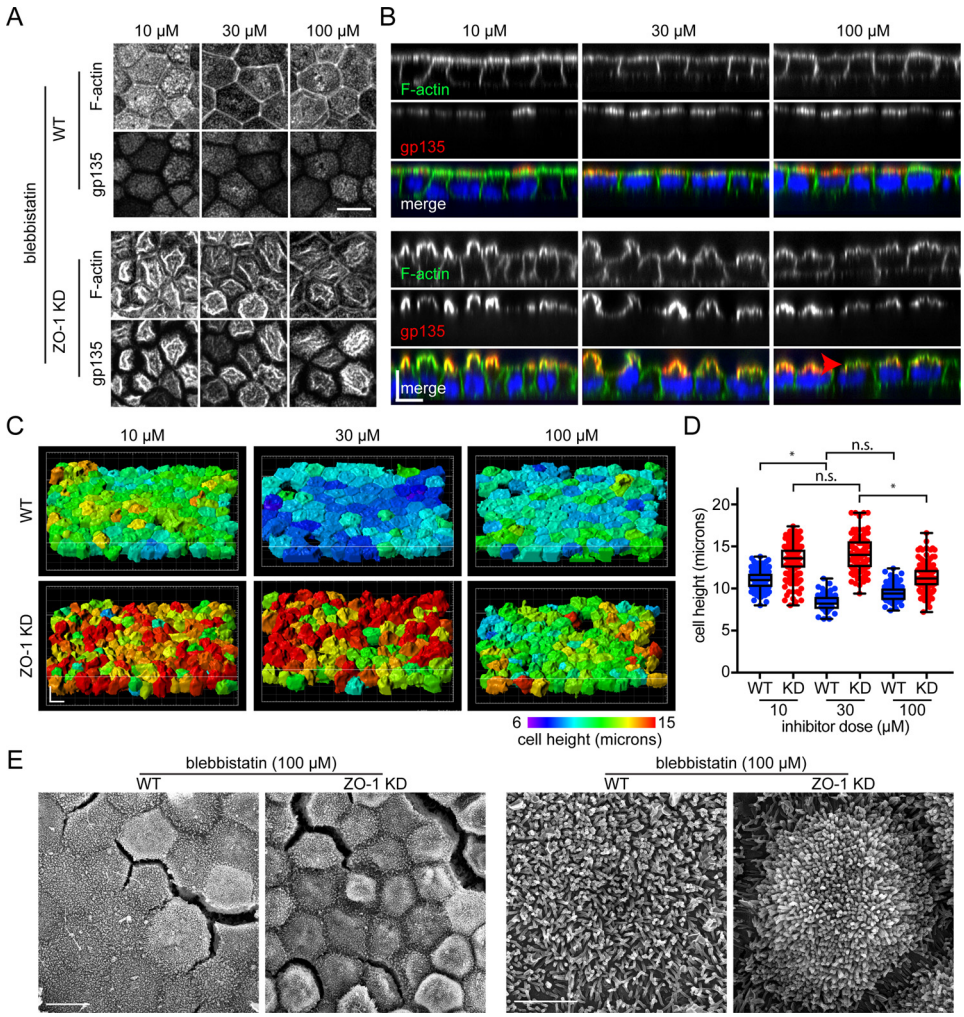

Figure 7. Blebbistatin-mediated inhibition of myosin-II ATPase activity reduces ZO-1 KD cell height and partially restores uniform apical surfaces. *A* and *B*, confluent WT and ZO-1 KD monolayers were subjected to calcium switch and treated with 10, 30, or 100 μM blebbistatin upon calcium repletion. Monolayers were stained for F-actin (phalloidin; *green*), podocalyxin/gp135 (*red*), and nuclei (Hoechst; *blue*). Representative maximal projections of full-monolayer thickness *z*-stacks and *x,z* projections are shown. *Red arrowhead*, ruffled apical membrane in 100 μM-treated ZO-1 KD monolayer. All images for a given antigen and image orientation are scaled identically. *Bars*, 10 μm. *C*, 3D renderings of individual cells were generated using F-actin as a membrane marker. Cells are *colored* based on cell height, as indicated. *Bar*, 10 μm. *D*, height of each 3D cell rendering was determined. The *box* encloses the second and third quartiles, the *center bar* indicates the mean, and *bars* extend to maximum and minimum values. Data are from one experiment representative of three independent studies. For WT, $n = 176$, 93, and 104, and for KD, $n = 189$, 102, and 122 for 10, 30, and 100 μM, respectively. *n.s.*, $p > 0.05$; *, $p < 0.001$ by one-way ANOVA with Kruskal–Wallis post-test for comparison indicated by *brackets*. *E*, scanning electron micrographs of WT and ZO-1 KD monolayers treated with blebbistatin for 24 h after calcium switch. *Bar*, 10 μm (*left*) and 3 μm (*right*).

Inhibition of F-actin polymerization, myosin motor activity, and dynamin II restores apical epithelial structure in vivo

The ability of F-actin disruption, myosin motor perturbation, and dynamin inhibition to restore cortical F-actin organization and reduce apical membrane expansion *in vitro* was striking. To determine whether these agents were also able to rescue morphology *in vivo*, a segment of intestine was functionally isolated while maintaining the neurovascular supply and cannulated. The lumen was perfused with saline containing latA, blebbistatin, BDM, dynasore, or vehicle (Fig. 10*A*). Examination of tissue sections showed that only latA substantially affected overall intestinal morphology; it induced extensive epithelial shedding in both WT or ZO-1 KO mice. As a result, whole mounts of latA-treated intestines were not amenable to 3D reconstruction.

Without exception, none of the drugs markedly affected apical membrane structure and F-actin organization in WT mice. However, all four drugs corrected apical expansion *in vivo* and resulted in unified apical surfaces without disruption at depressed cell–cell junctions (Fig. 10*B*). Confocal microscopy of jejunal whole mounts confirmed that BDM, blebbistatin, and dynasore all restored continuous flat apical surfaces but had no effect on WT epithelium (Fig. 10*C*). These *in vivo* data support the *in* vitro data and, when taken together, indicate that epithelial architectural abnormalities induced by ZO-1 deletion can be normalized by disrupting F-actin polymerization, myosin motor ATPase activity, or dynamin-mediated vesicle trafficking.

Discussion

Epithelial surfaces are critical sites that separate organisms from the external world or define interfaces between distinct internal compartments. These functions require that many epithelial cells work as a single unit. Organization of the basal aspect of these cells is maintained by interactions with the base-

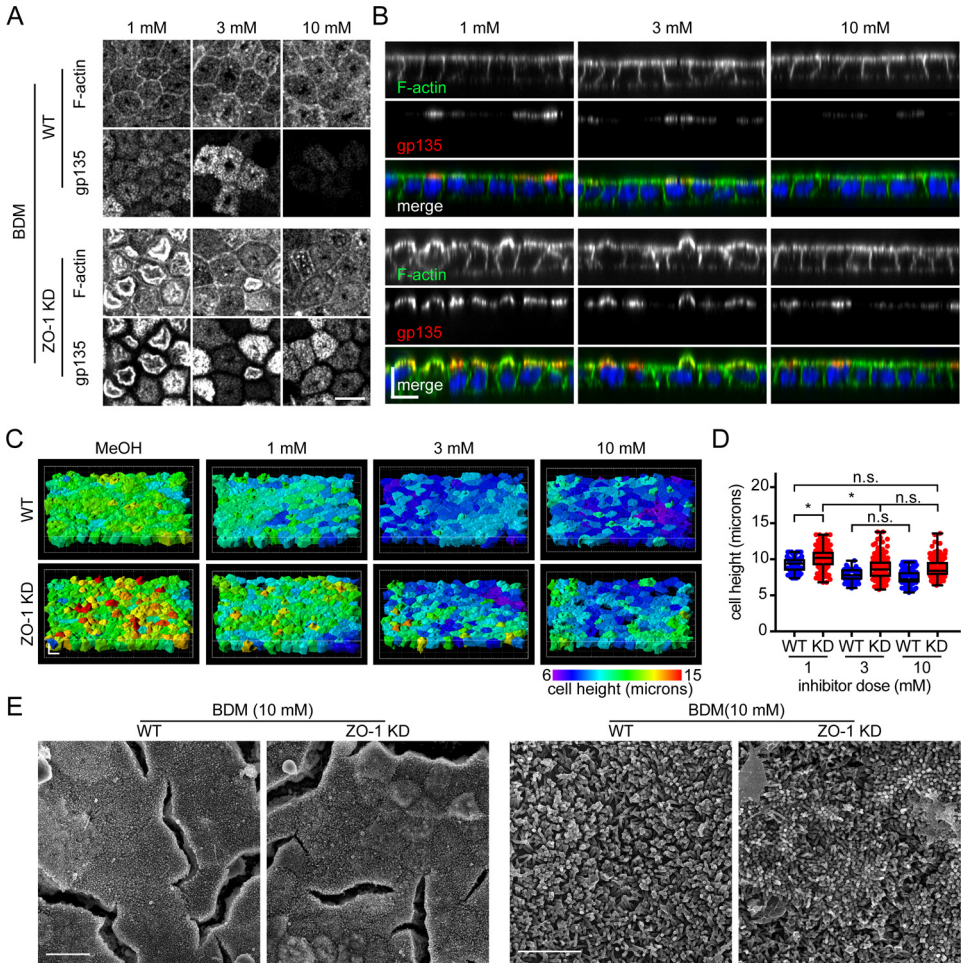

Figure 8. Inhibition of myosin ATPase activity restores a uniform apical surface in ZO-1 KD monolayers. *A* and *B*, confluent WT and ZO-1 KD monolayers were subjected to calcium switch and treated with 1, 3, or 10 mM BDM upon calcium repletion. Monolayers were then stained for F-actin (phalloidin; *green*), podocalyxin/gp135 (*red*), and nuclei (Hoescht; *blue*). Representative maximal projections of full-monolayer thickness *z*-stacks and *x,z* projections are shown. All images for a given antigen and image orientation are scaled identically. *Bars*, 10 μm. *C*, 3D renderings of individual cells were generated using F-actin as a membrane marker. Cells are *colored* based on cell height as indicated. *Bar*, 10 μm. *D*, height of each 3D cell rendering was determined. The *box* encloses the second and third quartiles, the *center bar* indicates the mean, and *bars* extend to maximum and minimum values. Data are from one experiment representative of three independent studies. For WT, $n = 164$, 186, and 192, and for KD, $n = 198$, 166, and 160 for 1, 3, and 10 mM, respectively. *n.s.*, $p > 0.05$; *, $p < 0.001$ by one-way ANOVA with the Kruskal–Wallis post-test for comparison indicated by *brackets*. *E*, scanning electron micrographs of WT and ZO-1 KD monolayers treated with BDM for 24 h after calcium switch. *Bar*, 10 μm (*left*) and 3 μm (*right*).

ment membrane. However, the factors that coordinate apical surfaces are less well-defined. The widespread presence of uniform apical surfaces, loss of which is well-recognized as a marker of neoplasia, argues that conservation of this single integrated multicellular surface structure is important to epithelial function. Here, we examined the contributions of the apical junctional complex protein ZO-1 to epithelial surface contiguity and apical membrane structure. Our data show that ZO-1 deficiency results in accumulation of dense cytoplasmic F-actin rings that define broad-based apical extensions. We further show that specific ZO-1 domains are required for normal structure, that absence of some domains can be complemented by ZO-2, and that inhibitors of myosin motor ATPase activity and membrane traffic can largely restore apical structure *in vitro* and *in vivo*.

Surprisingly, our data indicate that the ZO-1 ABR is not required for ZO-1–dependent organization of apical actomyosin. We considered the possibility that ZO-1/ZO-2 heterodimers could allow the ZO-2 ABR to complement deletion of that domain within ZO-1. However, ZO-1$^{\Delta ABR}$ was able to restore normal apical structure in ZO-1/ZO-2 double-KD monolayers. Similarly, the GuK domain was not required for rescue of actomyosin organization in ZO-1 KD or ZO-1/ZO-2 double-KD monolayers. Whereas ZO-1$^{\Delta PDZ1}$ expression corrected apical defects in ZO-1 KD monolayers when expressed at low levels, it was ineffective when expressed at high levels. Further, ZO-1$^{\Delta PDZ1}$ was unable to rescue ZO-1/ZO-2 double-KD monolayers. This suggests that ZO-2 PDZ1 domains complemented ZO-1$^{\Delta PDZ1}$, likely due to heterodimerization between ZO-1 and ZO-2. The requisite role of the PDZ1 domain suggests that ZO-1 interactions with claudins, which bind PDZ1, may be critical to regulation of normal apical structure. Disruption of ZO-1 interactions with other binding partners, including connexins and vinculin (63–66), which bind to PDZ2 and PDZ3 domains, respectively, could also be considered. Because we did not specifically test ZO-1 mutants lacking those domains, our data do not address this issue, which could be a topic of future studies.

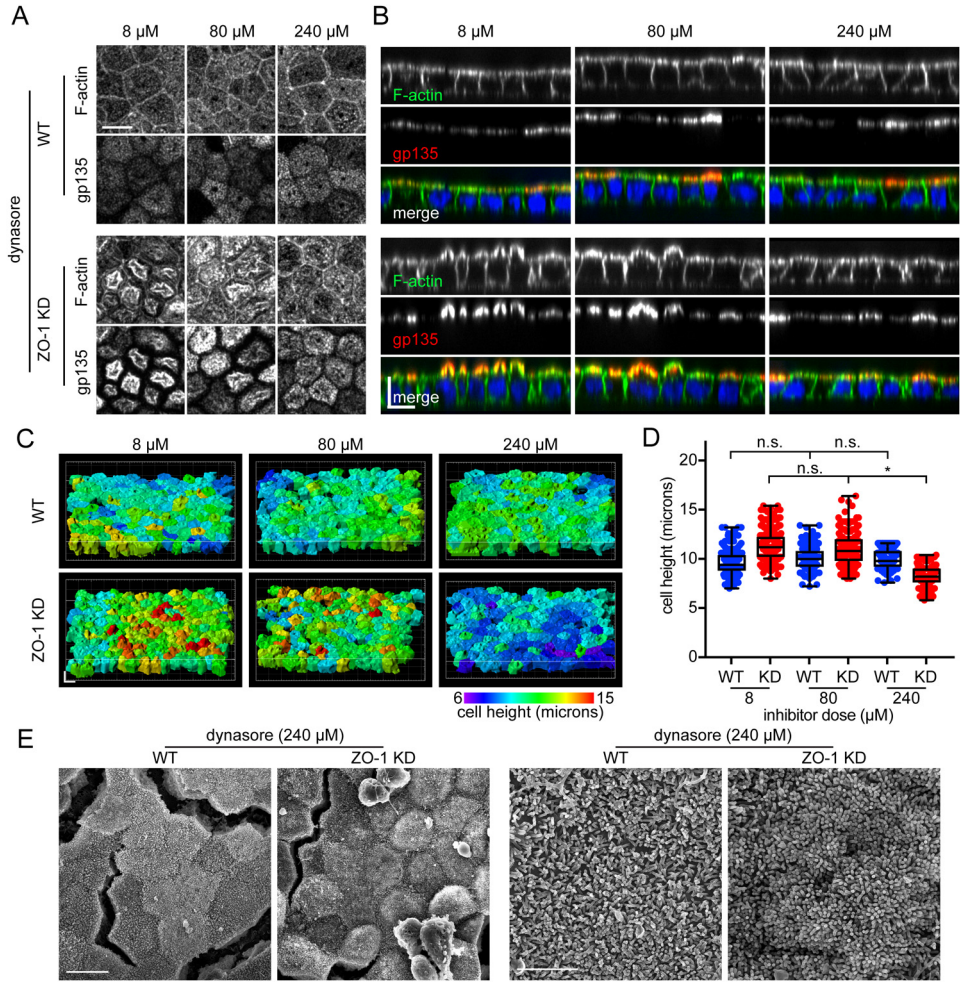

Figure 9. Dynamin II inhibition restores a uniform apical surface in ZO-1 KD monolayers. *A* and *B*, confluent WT and ZO-1 KD monolayers were subjected to calcium switch and treated with 8, 80, or 240 μM dynasore upon calcium repletion. Monolayers were then stained for F-actin (phalloidin; *green*), podocalyxin/gp135 (*red*), and nuclei (Hoechst; *blue*). Representative maximal projections of full-monolayer thickness *z*-stacks and *x*,*z* projections are shown. All images for a given antigen and image orientation are scaled identically. *Bars*, 10 μm. *C*, 3D renderings of individual cells were generated using F-actin as a membrane marker. Cells are *colored* based on cell height, as indicated. *Bar*, 10 μm. *D*, height of each 3D cell rendering was determined. The *box* encloses the second and third quartiles, the *center bar* indicates the mean, and *bars* extend to maximum and minimum values. Data are from one experiment representative of three independent studies. For WT, $n = 159$, 167, and 123, and for KD, $n = 190$, 150, and 122 for 8, 80, and 240 μM, respectively. *n.s.*, $p > 0.05$; *, $p < 0.001$ by one-way ANOVA with Kruskal–Wallis post-test for comparison indicated by *brackets*. *E*, scanning electron micrographs of WT and ZO-1 KD monolayers treated with BDM for 24 h after calcium switch. *Bar*, 10 μm (*left*) and 3 μm (*right*).

Similar data indicate that ZO-2 expression complements ZO-1$^{\Delta U5}$, as low-level expression rescued apical abnormalities in ZO-2–expressing monolayers but not in double-KD monolayers. Strikingly, high-level ZO-1$^{\Delta U5}$ expression exacerbated apical abnormalities in ZO-1 KD, but not double-KD, monolayers. This can be best explained as a dominant-negative effect of ZO-1$^{\Delta U5}$ on ZO-2 and suggests that, whereas the U5 domain is important to apical structure, the ZO-2 U5 domain can partially compensate for loss of that domain within ZO-1.

ZO-1 deletion induces polymerization of dense F-actin structures beneath the apical membrane. These are distinct from the dense perijunctional F-actin accumulations reported previously in ZO-1/ZO-2 double-KD monolayers (27), which were not seen in ZO-1 KO intestinal epithelia or ZO-1 single-KD monolayers. Notably, latA doses that eliminated cytoplasmic F-actin rings while having milder effects on perijunctional F-actin were able to significantly correct apical abnormalities within ZO-1 KD monolayers. Further, myosin motor ATPase inhibitors (blebbistatin and BDM) also restored apical cell structure and eliminated cytoplasmic F-actin rings without disrupting perijunctional F-actin in ZO-1 KD monolayers. Perfusion of blebbistatin or BDM through the intestinal lumen verified that these drugs had the same restorative effect on intestinal epithelia *in vivo*.

Given the lack of requirement for the ZO-1 ABR in generating normal apical structure, it is not entirely clear how ZO-1 deficiency so negatively impacts apical F-actin structures. However, a recent report examining the conformation of ZO-1 may provide some insight (67). That study showed that ZO-1 normally assumes an elongated molecular structure and is precisely oriented at apical junctional complexes. Simultaneous KD of ZO-2 and myosin motor ATPase inhibition with blebbistatin allowed ZO-1 to relax into a folded structure in which N and C termini were in proximity to one another (67). Neither blebbistatin nor ZO-2 KD alone were able to cause this change in ZO-1 confirmation. Thus, ZO-2 and cytoskeletal tension were both required for ZO-1 elongation. One could hypothesize that, in turn, ZO-1 regulates the magnitude of cytoskeletal

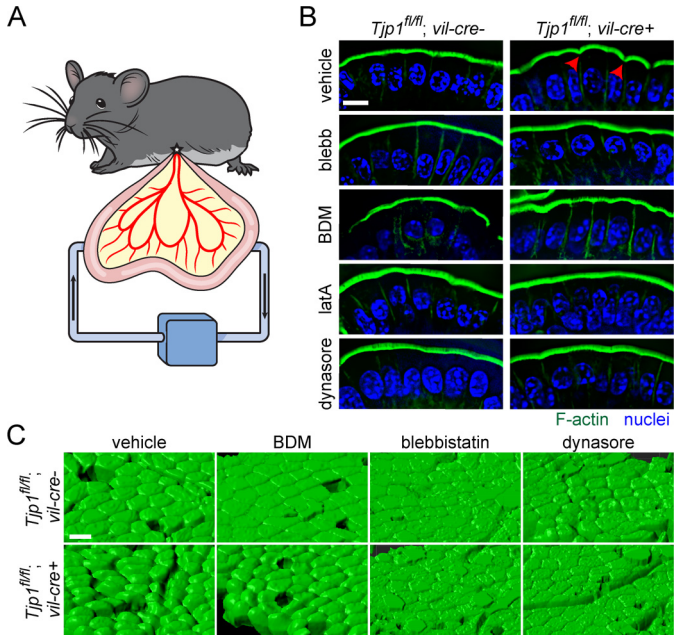

Figure 10. Inhibition of actin polymerization, myosin ATPase, or dynamin II restores community borders in ZO-1 KO intestinal epithelia *in vivo*. *A*, diagram depicting the *in vivo* perfusion assay. *B*, whole mounts of treated small intestines were stained for F-actin (phalloidin; *green*) and nuclei (Hoechst; *blue*). *x,z* projections are depicted here. *Arrows*, sites where a unified border is disrupted. Such areas are absent in WT epithelia and drug-treated ZO-1 KO epithelia. *Bar*, 10 μm. *C*, 3D cellular reconstructions of confocal *z*-stacks of whole mounts of small intestinal epithelia treated with the indicated drug. Cellular reconstructions could not be created for latA-treated intestines due to marked cellular disruption. *Bar*, 7.5 μm.

tension. This would predict that ZO-1 deletion could lead to dysregulated and excessive cytoskeletal tension that ultimately caused the apical abnormalities reported here.

Although we did not identify a specific protein, one potential effector within this signaling platform is the small GTPase Cdc42, which regulates tight junction assembly and vesicle trafficking in polarized epithelia (68, 69). Consistent with this, a guanine nucleotide exchange factor, Dbl3, positions Cdc42 along the lateral membrane to regulate apical surface size and shape (70). In a more recent report, the same authors speculated that, in addition to promoting apical myosin activation, Cdc42 may reduce perijunctional actomyosin contractility, which results in a contractility gradient that promotes apical expansion (71). Support for that interpretation included the observation that Cdc42 inhibition prevented apical expansion. In contrast, we found that Cdc42 inhibition exacerbated apical surface expansion of ZO-1 KD monolayers (Fig. S3). It is therefore unlikely that the phenotype induced by ZO-1 KO or KD is due to Cdc42 hyperactivation, as occurs after Dbl3 overexpression (71).

Perturbation of vesicular trafficking could provide an alternative mechanism for the apical expansion that occurs in ZO-1–deficient epithelia. Although ZO-1 has not been linked directly to regulation of membrane traffic, it is notable that key components of the exocyst are known to localize to tight junctions (72). Moreover, epithelia with endosomal maturation defects developed expanded apical surfaces similar to those in ZO-1–deficient cells (73). Consistent with this hypothesis, dynamin inhibition completely restored apical surface biogenesis in ZO-1–deficient epithelia, both *in vitro* and *in vivo*.

Membrane traffic defects could also contribute to the strikingly abnormal microvillus structure seen in ZO-1–deficient epithelia. One potential mechanism could be defects in vesicle release from microvillus tips (24). This would be consistent with the bizarre elongated microvilli we observed. Although microvillus structure was not the focus of our investigation, the diameter of these extensions, which was approximately half of that of the microvilli from which they arose, would be consistent with a lack of F-actin cores. This contrasts sharply with the relatively normal diameter of the modestly elongated microvilli described in Myo1a KO mice, which display excessive vesicle release (25), as well as the abnormal microvilli induced by *in vitro* protocadherin 24 KD (74). Notably, microvillus architecture was improved by inhibition of myosin motor activity or dynamin, but not by F-actin disruption. Regardless of the mechanism, it is difficult to rationalize the apical expansion and abnormal microvillus structure of ZO-1–deficient epithelial because ZO-1 is not present in apical membranes or microvilli. One potential explanation could relate to the as yet undefined function of the large, soluble, extrajunctional ZO-1 pool, which has been estimated to represent 60% of total ZO-1 (25, 74, 75). Overall, our data demonstrate an integral role of ZO-1 in regulating structure of apical membranes, subapical actomyosin, microvilli, and, above all, the unified single surface that epithelial sheets present to the external milieu.

Experimental procedures

Mice

To generate mice with intestinal epithelial-specific ZO-1 deletion, *Tjp1^{tm2a}(KOMP)Wtsi* (MGI:98759) C57BL/6N mice were bred with *B6.Cg-Tg(ACTFLPe)9205Dym/J* (MGI: 2448985) to delete the En2SA-LacZ-neo cassette between the Frt sites, thereby creating the *B6-Tjp1^{tm2a}* line. For experimental use, *B6.Cg-Tjp1^{tm2a}* mice were bred with *Tg(Vil-cre)20Syr* (MGI:3053819) mice to induce intestinal epithelial-specific gene deletion. *ZO-1$^{fl/fl}$; vil-cre^{+}* and *ZO-1$^{fl/fl}$; vil-cre^{-} mice* were maintained on a C57BL/6J background. Knockout was confirmed by Western blotting and immunohistochemistry, as shown in the figures, as well as routine genotyping. Mice of both sexes were used between 8 and 12 weeks of age. Littermates were used for individual experiments. All studies were performed according to protocols approved by institutional animal care and use committees of the University of Chicago, Brigham and Women's Hospital, Boston Children's Hospital, and Harvard Medical School. Animals were maintained in specific pathogen-free environments.

Intestinal perfusion assay

In vivo perfusion was performed as described previously (76). Briefly, adult, 8–12-week-old mice were fasted for 12–16 h before each experiment, and surgical plane anesthesia was induced with ketamine and xylazine. The abdomen was opened by a midline incision, and a 4–5-cm loop of jejunum was cannulated at the proximal and distal ends with 0.76-mm internal diameter polyethylene tubing. The lumen was flushed by perfusion with 140 mM NaCl, 10 mM HEPES, pH 7.4, warmed to

37 °C at 1 ml/min for 10 min using a peristaltic pump. This was replaced by fresh perfusion solution with or without 100 μM blebbistatin, 10 mM BDM, 240 μM dynasore, or 0.5 μM latA, and perfusion continued in a recirculating manner at 1 ml/min for 2 h. The abdominal cavity was covered with moistened gauze, and body temperature was maintained at 37 °C using a heat lamp. After perfusion, the animal was sacrificed, and the perfused jejunal segment was excised, fixed in 10% formalin, and embedded in paraffin or used for whole-mount preparation, as described below.

Cell lines and tissue culture

MDCK cells derived from the T23 MDCK clone were maintained in low glucose (1 g/liter) Dulbecco's modified Eagle's medium (LDMEM) supplemented with 10% fetal bovine serum, 15 mM HEPES, 250 mg/liter G418 (Gemini Bio-Products), and 1 μg/ml puromycin (Fisher Scientific) (77). ZO-1 KD MDCK cells (clone 4D3) and ZO-2 KD MDCK cells (clone 1C5) were cultured in T23 medium containing 30 μg/ml zeocin (Invitrogen) to select for cells expressing anti-ZO-1 and anti-ZO-2 shRNA (78). ZO-1/ZO-2 double-KD MDCK cells (clone 3B3) were cultured in T23 medium containing 30 mg/liter zeocin and 10 mg/liter blasticidin (27).

Cell lines expressing free EGFP or N-terminally tagged EGFP-ZO-1 constructs were generated as described previously (18). Briefly, DNA encoding human ZO-1 was mutated to evade shRNA targeting. Deletion constructs contained the following amino acid deletions: ZO-1$^{\Delta U5\text{-}GuK}$ (aa 591–803), ZO-1$^{\Delta ABR}$ (aa 1159–1383), ZO-1$^{\Delta U5\text{-}GuK\Delta ABR}$ (aa 591–803 and 1159–1383), ZO-1$^{\Delta U5}$ (aa 585–622), ZO-1$^{\Delta GuK}$ (aa 646–692), ZO-1$^{\Delta PDZ1}$ (aa 1–110). Deletion mutants were cloned into a PiggyBAC plasmid with an N-terminally tagged EGFP downstream of a tetracycline-responsive promoter (System Biosciences, Mountain View, CA). Plasmids were transfected into both ZO-1 KD and ZO-1/ZO-2 double-KD cells. Cells were maintained in their parental cell line medium supplemented with 50 μg/ml hygromycin B for transgene selection and 25 ng/ml doxycycline to repress transgene expression. Doxycycline was removed the day before plating for experiments and withheld from medium throughout experiments.

Occludin KD MDCK (clones F36 and F52) were cultured in T23 medium containing 50 μg/ml hygromycin B to prevent loss of occludin shRNA (79). Shroom2 KD and α-catenin KD MDCK cells were cultured in T23 medium containing 10 μg/ml blasticidin (18). All cell lines used in this study tested negative for mycoplasma contamination either at time of cell line acquisition or generation and again at 3-month intervals while being used.

Calcium switch assay

For growth on Transwell filters, cells were plated at a density of 150,000 cells on 0.33-cm^2 surface area, 0.4-μm pore Transwell filters (Corning) in 24-well plates. Growth medium was exchanged 48 h after plating. Calcium was depleted after 72 h of culture by washing, followed by incubation in calcium-free suspension-modified Eagle's medium (SMEM, Life Technologies) containing 10% dialyzed fetal bovine serum (Life Technologies) and 15 mM HEPES. After a 16-h incubation, calcium-free medium was replaced with normal LDMEM containing calcium. For pharmacologic inhibitor treatments, monolayers were exposed to the indicated doses of inhibitors upon calcium repletion and cultured with inhibitors for 24 h in the presence of calcium before fixation and immunostaining.

Immunofluorescence

Monolayers were fixed at the indicated time points in either ethanol (to visualize myosin IIB) or paraformaldehyde (to visualize all other assessed proteins). For ethanol fixation, monolayers were rinsed with and then submerged in −20 °C ethanol for 30 min. Subsequent steps were described previously (59). Briefly, cells were incubated in bis(sulfosuccinimidyl)suberate in PBS$^+$ (PBS containing 0.1% *n*-octyl-glutaraldehyde) for 30 min. Monolayers were washed in PBS$^+$, quenched with 100 mM ethylenediamine, and washed again in PBS$^+$. Inserts were then blocked for 1 h at room temperature in blocking buffer containing 1% nonfat milk, 1% fish gelatin, and 1% BSA in PBS$^+$. For PFA fixation, cells were rinsed in PBS and incubated in 4% PFA for 20 min at room temperature. Fixation was quenched by a 15-min incubation with 50 mM NH_4Cl, and cells were permeabilized with 0.5% Triton X-100 for 10 min. Monolayers were blocked with 10% normal goat serum in PBS for 1 h at room temperature. Primary antibodies were diluted in blocking buffer and incubated overnight at 4 °C. Primary antibodies were washed, and monolayers were incubated with a 1:100 dilution of the appropriate Alexa Fluor 488–, 594–, or 647–conjugated donkey anti-rabbit, -mouse, or rat F(ab′)$_2$ AffiniPure antiserum secondary antibodies (Jackson Immunoresearch) for 1 h at room temperature. F-actin and nuclei were labeled with Alexa Fluor–conjugated phalloidin and Hoechst 33342, respectively. Monolayers were mounted under coverslips in Slowfade Diamond (Life Technologies).

Sections (5 μm) of paraffin-embedded intestinal tissues were collected on coated slides and deparaffinized. Antigen retrieval used pH9 Target Retrieval Solution (Agilent Technologies, catalog no. S2367) for 40 min at 95 °C. After blocking nonspecific binding with 1% normal donkey serum in PBS, sections were incubated overnight with rabbit anti-NHE3, mouse anti-E-cadherin, and rat anti-ZO-1. After washing, sections were incubated for 2 h with Alexa Fluor 488–, Alexa Fluor 594–, and Alexa Fluor 647–conjugated donkey anti-rabbit, -mouse, and -rat F(ab′)$_2$ AffiniPure antisera (Jackson Immunoresearch) and Hoechst 33342 (Invitrogen). After washing, ProLong Diamond antifade reagent (Life Technologies) was added, and coverslips were applied.

Small intestinal whole mounts were prepared for fluorescent imaging as follows. Animals were sacrificed in accordance with institutional animal care and use committee protocols. A segment of jejunum was excised, cut lengthwise to expose the luminal surface, and then incubated in fixative (0.5% paraformaldehyde, 15% picric acid, and 0.1 M sodium phosphate buffer (pH 7.0)) with gentle shaking for 12 h at 4 °C. Specimens were rinsed in ice-cold PBS (three washes, 5 min each), followed by a 3-h incubation in 10% sucrose, 0.1% NaN_3/PBS (4 °C) and an overnight incubation in 20% sucrose, 10% glycerol, 0.1% NaN_3/PBS (4 °C). A 1-cm portion of the fixed intestinal segment was washed in PBS and blocked in 0.5% BSA, 0.1% NaN_3, 0.3% Tri-

ton X-100, 5% normal donkey serum/PBS for 6 h. Tissues were stained with phalloidin (Invitrogen) and Hoechst 33342 overnight at 4 °C, followed by five 0.3% Triton X-100/PBS washes (1 h per cycle, 4 °C). Sections were washed with cold PBS twice for 10 min each and immersed in 2% PFA/PBS for 2 days at 4 °C. The stained whole-mount preparation was placed on a glass slide (villus side up) with imaging spacer (Grace Bio-Labs), and Slowfade Diamond antifade reagent (Life Technologies) was added, followed by a coverslip.

Microscopy

Tissue sections were imaged using an Axioplan 2 (Zeiss) microscope, Chroma single channel ET filter sets, ×20 numerical aperture 0.8 Plan-Apochromat and ×100 numerical aperture 1.3 Plan-Neofluar oil immersion objectives, and a Coolsnap HQ camera (Photometrics) controlled by Metamorph version 7. Image stacks (0.2-μm z-steps) were deconvoluted using Autoquant X3 (MediaCybernetics).

Confocal images of cultured monolayers and intestinal whole mounts were acquired on a Leica DMI6000 microscope equipped with a CSUX Yokogawa spinning disk (Andor Technologies). Laser illumination was supplemented with Borealis illumination technology to ensure uniform illumination across the sample, images were acquired using either a Retiga EXi Fast 1394 (QImaging) or Zyla 4.2 Plus sCMOS (Andor Technologies) camera, and the system was controlled by Metamorph 7. A ×20 HC PLAN Apo/0.70 objective (Leica 11506166) was used to capture z-stacks with 0.5-μm z-steps, and both ×63 HCX PL Apo/1.3 glycerol immersion (Leica 506193) and ×100 HC PLAN Apo/1.4 oil immersion (Leica 11506372) objectives were used to capture z-stacks with 0.2-μm z-steps. Identical laser intensity, exposure time, and camera gain settings were used to acquire all images of a given fluorescent wavelength or label within individual experiments. After acquisition, select images were deconvoluted where indicated using Autoquant X3. All images were then scaled and cropped, maximal and x,z projections were created in MetaMorph (Molecular Devices), and rendering and quantification were performed in Imaris version 8.4.1 (Bitplane) as described below. All images are representative of at least three independent experiments.

Confocal z-stack reconstruction and quantification

To generate 3D reconstructions of both intestinal whole mounts and cultured monolayers, confocal z-stacks were viewed and processed with the surface tool, spots tool, or cell module in Imaris.

The surface tool was used to render the apical surface of both intestinal whole mounts and cultured monolayers. First, a region of interest that spanned from immediately basal to the tight junction to just above the apical-most point of the surface was drawn. Next, a surface was built within the region of interest using F-actin as a marker with the following creation parameters: smoothing, grain size 0.125 and 0.5 μm (whole mount and cultured monolayer, respectively), without background subtraction. Thresholding was performed manually for each surface rendered.

For cell creation, F-actin (phalloidin) was used as a membrane marker with the following creation parameters: smallest cell diameter 1.28 and 5 μm (whole mount and monolayer, respectively), membrane detail 0.128 and 0.227 μm (whole mount and monolayer, respectively), and local contrast filter. Intensity and quality measurements were manually thresholded to generate representative renderings. After initial cell generation, cells at the edges of the region of interest (in the x and y directions) and cell renderings that were not within the plane of the epithelium (in the z direction) were eliminated by filtering. The height of each resulting cell rendering was calculated with a bounding box in the z direction and is reported along with cell population statistics. Cells are color-coded by cell height using the same scale for all monolayers.

Scanning EM

Confluent monolayers were rinsed with warm LDMEM without additives and fixed for 1 h at room temperature with 3% glutaraldehyde in 0.1 M sodium cacodylate buffer with 50 mM $CaCl_2$ (pH 7.4). Fixed cells were rinsed three times for 5 min with 0.1 M sodium cacodylate buffer before a 30-min incubation with 1% osmium tetroxide in 0.1 M sodium cacodylate buffer. Cells were rinsed with water and then incubated for 20 min with 2% tannic acid in water. Monolayers were rinsed with water again before a 20-min incubation with 1% osmium tetroxide in water. Samples were then dehydrated with a series of 10-min ethanol washes (30, 50, 75, 100, and 100%) and dried overnight in a chemical hood with hexamethyldisilazane. Whole-mount intestinal tissue samples were prepared by the same method, but before fixation, intestines were flushed with 37 °C Hanks' balanced salt solution, cut lengthwise to expose the mucosal surface, and fixed overnight at 4 °C. A Ted Pella sputter coater was used to sputter monolayer and tissue samples with 8 and 10 nm of platinum-palladium alloy, respectively. All images were acquired in the University of Chicago Materials Research Center using an FEI Nova NanoSEM 230 at 10.0 kV using a TLD detector and a 45-μs dwell time.

Transmission EM

For transmission EM, tissue samples were prepared as described previously (80). Briefly, tissues were fixed with 2.5% glutaraldehyde and 4% PFA in 0.1 M sodium cacodylate buffer. Samples were dehydrated and embedded in Spurr resin prior to sectioning. Images were acquired on an FEI Tecnai F30 transmission electron microscope in the Advanced Electron Microscopy Facility at the University of Chicago.

Western blotting

Cell lysates were taken from confluent monolayers in nonreducing sample buffer (0.375 M Tris base, 15% glycerin, 3% SDS, pH 6.8) with 1:200 Protease Inhibitor Mixture Set III (EMD Millipore). Samples were boiled for 5 min followed by sonication on ice. 15 μg of lysate was loaded per lane and separated by SDS-PAGE. Protein was then transferred to PVDF membranes as described previously (80). PVDF membranes were blocked with 5% milk in TBST for 1 h, and the indicated proteins were probed with primary antibodies at the dilutions shown in Table S1. Species-specific horseradish peroxidase–conjugated sec-

ondary antibodies were used, and proteins were detected by chemiluminescence.

Author contributions—M. A. O. and J. R. T. conceived of the project. M. A. O., W. C., W.-T. K., L. S., A. S. F., and J. R. T. designed the experiments. M. A. O., W. C., W.-T. K., G. S., A. S., Y. W., and J. R. T. performed the experiments.

Acknowledgments—We are grateful to Dr. Vytas Bindokas (University of Chicago) for outstanding advice as well as the staffs of the Integrated Light Microscopy Core Facility, Electron Microscopy Core Facility, and Scanning Electron Microscopy Core Facility at the University of Chicago for invaluable assistance.

References

1. Shashikanth, N., Yeruva, S., Ong, M. L. D. M., Odenwald, M. A., Pavlyuk, R., and Turner, J. R. (2017) Epithelial organization: the gut and beyond. *Compr. Physiol.* **7,** 1497–1518 Medline
2. Allen, T. D., and Potten, C. S. (1976) Significance of cell shape in tissue architecture. *Nature* **264,** 545–547 CrossRef Medline
3. Fernandez-Gonzalez, R., and Zallen, J. A. (2009) Cell mechanics and feedback regulation of actomyosin networks. *Sci. Signal.* **2,** pe78 Medline
4. Sawyer, J. M., Harrell, J. R., Shemer, G., Sullivan-Brown, J., Roh-Johnson, M., and Goldstein, B. (2010) Apical constriction: a cell shape change that can drive morphogenesis. *Dev. Biol.* **341,** 5–19 CrossRef Medline
5. Martin, A. C., Kaschube, M., and Wieschaus, E. F. (2009) Pulsed contractions of an actin-myosin network drive apical constriction. *Nature* **457,** 495–499 CrossRef Medline
6. Dietz, M. L., Bernaciak, T. M., Vendetti, F., Kielec, J. M., and Hildebrand, J. D. (2006) Differential actin-dependent localization modulates the evolutionarily conserved activity of Shroom family proteins. *J. Biol. Chem.* **281,** 20542–20554 CrossRef Medline
7. Plageman, T. F., Jr., Chauhan, B. K., Yang, C., Jaudon, F., Shang, X., Zheng, Y., Lou, M., Debant, A., Hildebrand, J. D., and Lang, R. A. (2011) A Trio-RhoA-Shroom3 pathway is required for apical constriction and epithelial invagination. *Development* **138,** 5177–5188 CrossRef Medline
8. Lee, J. Y., and Harland, R. M. (2010) Endocytosis is required for efficient apical constriction during *Xenopus* gastrulation. *Curr. Biol.* **20,** 253–258 CrossRef Medline
9. Eiraku, M., Takata, N., Ishibashi, H., Kawada, M., Sakakura, E., Okuda, S., Sekiguchi, K., Adachi, T., and Sasai, Y. (2011) Self-organizing optic-cup morphogenesis in three-dimensional culture. *Nature* **472,** 51–56 CrossRef Medline
10. Martin, A. C., and Goldstein, B. (2014) Apical constriction: themes and variations on a cellular mechanism driving morphogenesis. *Development* **141,** 1987–1998 CrossRef Medline
11. Lee, C. S., Choi, C. K., Shin, E. Y., Schwartz, M. A., and Kim, E. G. (2010) Myosin II directly binds and inhibits Dbl family guanine nucleotide exchange factors: a possible link to Rho family GTPases. *J. Cell Biol.* **190,** 663–674 CrossRef Medline
12. Grosse, A. S., Pressprich, M. F., Curley, L. B., Hamilton, K. L., Margolis, B., Hildebrand, J. D., and Gumucio, D. L. (2011) Cell dynamics in fetal intestinal epithelium: implications for intestinal growth and morphogenesis. *Development* **138,** 4423–4432 CrossRef Medline
13. Marchiando, A. M., Shen, L., Graham, W. V., Edelblum, K. L., Duckworth, C. A., Guan, Y., Montrose, M. H., Turner, J. R., and Watson, A. J. (2011) The epithelial barrier is maintained by *in vivo* tight junction expansion during pathologic intestinal epithelial shedding. *Gastroenterology* **140,** 1208–1218.e1–2 CrossRef Medline
14. Eisenhoffer, G. T., Loftus, P. D., Yoshigi, M., Otsuna, H., Chien, C. B., Morcos, P. A., and Rosenblatt, J. (2012) Crowding induces live cell extrusion to maintain homeostatic cell numbers in epithelia. *Nature* **484,** 546–549 CrossRef Medline
15. Rosenblatt, J., Raff, M. C., and Cramer, L. P. (2001) An epithelial cell destined for apoptosis signals its neighbors to extrude it by an actin- and myosin-dependent mechanism. *Curr. Biol.* **11,** 1847–1857 CrossRef Medline
16. Saw, T. B., Doostmohammadi, A., Nier, V., Kocgozlu, L., Thampi, S., Toyama, Y., Marcq, P., Lim, C. T., Yeomans, J. M., and Ladoux, B. (2017) Topological defects in epithelia govern cell death and extrusion. *Nature* **544,** 212–216 CrossRef Medline
17. Yu, D., Marchiando, A. M., Weber, C. R., Raleigh, D. R., Wang, Y., Shen, L., and Turner, J. R. (2010) MLCK-dependent exchange and actin binding region-dependent anchoring of ZO-1 regulate tight junction barrier function. *Proc. Natl. Acad. Sci. U.S.A.* **107,** 8237–8241 CrossRef Medline
18. Odenwald, M. A., Choi, W., Buckley, A., Shashikanth, N., Joseph, N. E., Wang, Y., Warren, M. H., Buschmann, M. M., Pavlyuk, R., Hildebrand, J., Margolis, B., Fanning, A. S., and Turner, J. R. (2017) ZO-1 interactions with F-actin and occludin direct epithelial polarization and single lumen specification in 3D culture. *J. Cell Sci.* **130,** 243–259 CrossRef Medline
19. Fanning, A. S., Ma, T. Y., and Anderson, J. M. (2002) Isolation and functional characterization of the actin binding region in the tight junction protein ZO-1. *FASEB J.* **16,** 1835–1837 CrossRef Medline
20. Katsuno, T., Umeda, K., Matsui, T., Hata, M., Tamura, A., Itoh, M., Takeuchi, K., Fujimori, T., Nabeshima, Y., Noda, T., Tsukita, S., and Tsukita, S. (2008) Deficiency of zonula occludens-1 causes embryonic lethal phenotype associated with defected yolk sac angiogenesis and apoptosis of embryonic cells. *Mol. Biol. Cell* **19,** 2465–2475 CrossRef Medline
21. Bryant, D. M., Datta, A., Rodríguez-Fraticelli, A. E., Peränen, J., Martín-Belmonte, F., and Mostov, K. E. (2010) A molecular network for de novo generation of the apical surface and lumen. *Nat. Cell Biol.* **12,** 1035–1045 CrossRef Medline
22. Roland, J. T., Bryant, D. M., Datta, A., Itzen, A., Mostov, K. E., and Goldenring, J. R. (2011) Rab GTPase-Myo5B complexes control membrane recycling and epithelial polarization. *Proc. Natl. Acad. Sci. U.S.A.* **108,** 2789–2794 CrossRef Medline
23. Vogel, G. F., Klee, K. M., Janecke, A. R., Müller, T., Hess, M. W., and Huber, L. A. (2015) Cargo-selective apical exocytosis in epithelial cells is conducted by Myo5B, Slp4a, Vamp7, and Syntaxin 3. *J. Cell Biol.* **211,** 587–604 CrossRef Medline
24. McConnell, R. E., Higginbotham, J. N., Shifrin, D. A., Jr., Tabb, D. L., Coffey, R. J., and Tyska, M. J. (2009) The enterocyte microvillus is a vesicle-generating organelle. *J. Cell Biol.* **185,** 1285–1298 CrossRef Medline
25. Tyska, M. J., Mackey, A. T., Huang, J. D., Copeland, N. G., Jenkins, N. A., and Mooseker, M. S. (2005) Myosin-1a is critical for normal brush border structure and composition. *Mol. Biol. Cell* **16,** 2443–2457 CrossRef Medline
26. Choi, W., Acharya, B. R., Peyret, G., Fardin, M. A., Mège, R. M., Ladoux, B., Yap, A. S., Fanning, A. S., and Peifer, M. (2016) Remodeling the zonula adherens in response to tension and the role of afadin in this response. *J. Cell Biol.* **213,** 243–260 CrossRef Medline
27. Fanning, A. S., Van Itallie, C. M., and Anderson, J. M. (2012) Zonula occludens-1 and -2 regulate apical cell structure and the zonula adherens cytoskeleton in polarized epithelia. *Mol. Biol. Cell* **23,** 577–590 CrossRef Medline
28. Balda, M. S., Garrett, M. D., and Matter, K. (2003) The ZO-1-associated Y-box factor ZONAB regulates epithelial cell proliferation and cell density. *J. Cell Biol.* **160,** 423–432 CrossRef Medline
29. Sourisseau, T., Georgiadis, A., Tsapara, A., Ali, R. R., Pestell, R., Matter, K., and Balda, M. S. (2006) Regulation of PCNA and cyclin D1 expression and epithelial morphogenesis by the ZO-1-regulated transcription factor ZONAB/DbpA. *Mol. Cell Biol.* **26,** 2387–2398 CrossRef Medline
30. Ikenouchi, J., Umeda, K., Tsukita, S., Furuse, M., and Tsukita, S. (2007) Requirement of ZO-1 for the formation of belt-like adherens junctions during epithelial cell polarization. *J. Cell Biol.* **176,** 779–786 CrossRef Medline
31. Fanning, A. S., and Anderson, J. M. (2009) Zonula occludens-1 and -2 are cytosolic scaffolds that regulate the assembly of cellular junctions. *Ann. N.Y. Acad. Sci.* **1165,** 113–120 CrossRef Medline
32. McNeil, E., Capaldo, C. T., and Macara, I. G. (2006) Zonula occludens-1 function in the assembly of tight junctions in Madin-Darby canine kidney epithelial cells. *Mol. Biol. Cell* **17,** 1922–1932 CrossRef Medline

33. Rodgers, L. S., Beam, M. T., Anderson, J. M., and Fanning, A. S. (2013) Epithelial barrier assembly requires coordinated activity of multiple domains of the tight junction protein ZO-1. *J. Cell Sci.* **126,** 1565–1575 CrossRef Medline
34. Etournay, R., Zwaenepoel, I., Perfettini, I., Legrain, P., Petit, C., and El-Amraoui, A. (2007) Shroom2, a myosin-VIIa- and actin-binding protein, directly interacts with ZO-1 at tight junctions. *J. Cell Sci.* **120,** 2838–2850 CrossRef Medline
35. Furuse, M., Itoh, M., Hirase, T., Nagafuchi, A., Yonemura, S., Tsukita, S., and Tsukita, S. (1994) Direct association of occludin with ZO-1 and its possible involvement in the localization of occludin at tight junctions. *J. Cell Biol.* **127,** 1617–1626 CrossRef Medline
36. Itoh, M., Nagafuchi, A., Moroi, S., and Tsukita, S. (1997) Involvement of ZO-1 in cadherin-based cell adhesion through its direct binding to α catenin and actin filaments. *J. Cell Biol.* **138,** 181–192 CrossRef Medline
37. Müller, S. L., Portwich, M., Schmidt, A., Utepbergenov, D. I., Huber, O., Blasig, I. E., and Krause, G. (2005) The tight junction protein occludin and the adherens junction protein α-catenin share a common interaction mechanism with ZO-1. *J. Biol. Chem.* **280,** 3747–3756 CrossRef Medline
38. Coué, M., Brenner, S. L., Spector, I., and Korn, E. D. (1987) Inhibition of actin polymerization by latrunculin A. *FEBS Lett.* **213,** 316–318 CrossRef Medline
39. Shen, L., Black, E. D., Witkowski, E. D., Lencer, W. I., Guerriero, V., Schneeberger, E. E., and Turner, J. R. (2006) Myosin light chain phosphorylation regulates barrier function by remodeling tight junction structure. *J. Cell Sci.* **119,** 2095–2106 CrossRef Medline
40. Turner, J. R., Rill, B. K., Carlson, S. L., Carnes, D., Kerner, R., Mrsny, R. J., and Madara, J. L. (1997) Physiological regulation of epithelial tight junctions is associated with myosin light-chain phosphorylation. *Am. J. Physiol.* **273,** C1378–C1385 CrossRef Medline
41. Nighot, M., Al-Sadi, R., Guo, S., Rawat, M., Nighot, P., Watterson, M. D., and Ma, T. Y. (2017) Lipopolysaccharide-induced increase in intestinal epithelial tight permeability is mediated by Toll-like receptor 4/myeloid differentiation primary response 88 (MyD88) activation of myosin light chain kinase expression. *Am. J. Pathol.* **187,** 2698–2710 CrossRef Medline
42. Kovács, M., Tóth, J., Hetényi, C., Málnási-Csizmadia, A., and Sellers, J. R. (2004) Mechanism of blebbistatin inhibition of myosin II. *J. Biol. Chem.* **279,** 35557–35563 CrossRef Medline
43. Limouze, J., Straight, A. F., Mitchison, T., and Sellers, J. R. (2004) Specificity of blebbistatin, an inhibitor of myosin II. *J. Muscle Res. Cell Motil.* **25,** 337–341 CrossRef Medline
44. Straight, A. F., Cheung, A., Limouze, J., Chen, I., Westwood, N. J., Sellers, J. R., and Mitchison, T. J. (2003) Dissecting temporal and spatial control of cytokinesis with a myosin II inhibitor. *Science* **299,** 1743–1747 CrossRef Medline
45. Ostap, E. M. (2002) 2,3-Butanedione monoxime (BDM) as a myosin inhibitor. *J. Muscle Res. Cell Motil.* **23,** 305–308 CrossRef Medline
46. Cramer, L. P., and Mitchison, T. J. (1995) Myosin is involved in postmitotic cell spreading. *J. Cell Biol.* **131,** 179–189 CrossRef Medline
47. Siegman, M. J., Mooers, S. U., Warren, T. B., Warshaw, D. M., Ikebe, M., and Butler, T. M. (1994) Comparison of the effects of 2,3-butanedione monoxime on force production, myosin light chain phosphorylation and chemical energy usage in intact and permeabilized smooth and skeletal muscles. *J. Muscle Res. Cell Motil.* **15,** 457–472 CrossRef Medline
48. Sellin, L. C., and McArdle, J. J. (1994) Multiple effects of 2,3-butanedione monoxime. *Pharmacol. Toxicol.* **74,** 305–313 CrossRef Medline
49. Zolotarevsky, Y., Hecht, G., Koutsouris, A., Gonzalez, D. E., Quan, C., Tom, J., Mrsny, R. J., and Turner, J. R. (2002) A membrane-permeant peptide that inhibits MLC kinase restores barrier function in *in vitro* models of intestinal disease. *Gastroenterology* **123,** 163–172 CrossRef Medline
50. Owens, S. E., Graham, W. V., Siccardi, D., Turner, J. R., and Mrsny, R. J. (2005) A strategy to identify stable membrane-permeant peptide inhibitors of myosin light chain kinase. *Pharm. Res.* **22,** 703–709 CrossRef Medline
51. Surviladze, Z., Waller, A., Strouse, J. J., Bologa, C., Ursu, O., Salas, V., Parkinson, J. F., Phillips, G. K., Romero, E., Wandinger-Ness, A., Sklar, L. A., Schroeder, C., Simpson, D., Noth, J., Wang, J., *et al.* (2010) A potent and selective inhibitor of Cdc42 GTPase. in *Probe Reports from the NIH Molecular Libraries Program*, National Institutes of Health, Bethesda, MD, available from: https://www.ncbi.nlm.nih.gov/books/NBK51965/
52. Uehata, M., Ishizaki, T., Satoh, H., Ono, T., Kawahara, T., Morishita, T., Tamakawa, H., Yamagami, K., Inui, J., Maekawa, M., and Narumiya, S. (1997) Calcium sensitization of smooth muscle mediated by a Rho-associated protein kinase in hypertension. *Nature* **389,** 990–994 CrossRef Medline
53. Barfod, E. T., Moore, A. L., Van de Graaf, B. G., and Lidofsky, S. D. (2011) Myosin light chain kinase and Src control membrane dynamics in volume recovery from cell swelling. *Mol. Biol. Cell* **22,** 634–650 CrossRef Medline
54. Chua, J., Rikhy, R., and Lippincott-Schwartz, J. (2009) Dynamin 2 orchestrates the global actomyosin cytoskeleton for epithelial maintenance and apical constriction. *Proc. Natl. Acad. Sci. U. S. A.* **106,** 20770–20775 CrossRef Medline
55. Yu, H. Y., and Bement, W. M. (2007) Multiple myosins are required to coordinate actin assembly with coat compression during compensatory endocytosis. *Mol. Biol. Cell* **18,** 4096–4105 CrossRef Medline
56. Carisey, A. F., Mace, E. M., Saeed, M. B., Davis, D. M., and Orange, J. S. (2018) Nanoscale dynamism of actin enables secretory function in cytolytic cells. *Curr. Biol.* **28,** 489–502.e9 CrossRef Medline
57. Tran, D. T., Masedunskas, A., Weigert, R., and Ten Hagen, K. G. (2015) Arp2/3-mediated F-actin formation controls regulated exocytosis *in vivo*. *Nat. Commun.* **6,** 10098 CrossRef Medline
58. Papadopulos, A. (2017) Membrane shaping by actin and myosin during regulated exocytosis. *Mol. Cell Neurosci.* **84,** 93–99 CrossRef Medline
59. Shen, L., and Turner, J. R. (2005) Actin depolymerization disrupts tight junctions via caveolae-mediated endocytosis. *Mol. Biol. Cell* **16,** 3919–3936 CrossRef Medline
60. Marchiando, A. M., Shen, L., Graham, W. V., Weber, C. R., Schwarz, B. T., Austin, J. R., 2nd, Raleigh, D. R., Guan, Y., Watson, A. J., Montrose, M. H., and Turner, J. R. (2010) Caveolin-1-dependent occludin endocytosis is required for TNF-induced tight junction regulation *in vivo*. *J. Cell Biol.* **189,** 111–126 CrossRef Medline
61. Macia, E., Ehrlich, M., Massol, R., Boucrot, E., Brunner, C., and Kirchhausen, T. (2006) Dynasore, a cell-permeable inhibitor of dynamin. *Dev. Cell* **10,** 839–850 CrossRef Medline
62. Park, R. J., Shen, H., Liu, L., Liu, X., Ferguson, S. M., and De Camilli, P. (2013) Dynamin triple knockout cells reveal off target effects of commonly used dynamin inhibitors. *J. Cell Sci.* **126,** 5305–5312 CrossRef Medline
63. Chen, J., Pan, L., Wei, Z., Zhao, Y., and Zhang, M. (2008) Domain-swapped dimerization of ZO-1 PDZ2 generates specific and regulatory connexin43-binding sites. *EMBO J.* **27,** 2113–2123 CrossRef Medline
64. Xiao, F., Weng, J., Fan, K., and Wang, W. (2011) Detailed regulatory mechanism of the interaction between ZO-1 PDZ2 and connexin43 revealed by MD simulations. *PLoS One* **6,** e21527 CrossRef Medline
65. Zemljic-Harpf, A. E., Godoy, J. C., Platoshyn, O., Asfaw, E. K., Busija, A. R., Domenighetti, A. A., and Ross, R. S. (2014) Vinculin directly binds zonula occludens-1 and is essential for stabilizing connexin-43-containing gap junctions in cardiac myocytes. *J. Cell Sci.* **127,** 1104–1116 CrossRef Medline
66. Giepmans, B. N., and Moolenaar, W. H. (1998) The gap junction protein connexin43 interacts with the second PDZ domain of the zona occludens-1 protein. *Curr. Biol.* **8,** 931–934 CrossRef Medline
67. Spadaro, D., Le, S., Laroche, T., Mean, I., Jond, L., Yan, J., and Citi, S. (2017) Tension-dependent stretching activates ZO-1 to control the junctional localization of its interactors. *Curr. Biol.* **27,** 3783–3795.e8 CrossRef Medline
68. Jaffe, A. B., Kaji, N., Durgan, J., and Hall, A. (2008) Cdc42 controls spindle orientation to position the apical surface during epithelial morphogenesis. *J. Cell Biol.* **183,** 625–633 CrossRef Medline
69. Rojas, R., Ruiz, W. G., Leung, S. M., Jou, T. S., and Apodaca, G. (2001) Cdc42-dependent modulation of tight junctions and membrane protein traffic in polarized Madin-Darby canine kidney cells. *Mol. Biol. Cell* **12,** 2257–2274 CrossRef Medline
70. Zihni, C., Munro, P. M., Elbediwy, A., Keep, N. H., Terry, S. J., Harris, J., Balda, M. S., and Matter, K. (2014) Dbl3 drives Cdc42 signaling at the apical margin to regulate junction position and apical differentiation. *J. Cell Biol.* **204,** 111–127 CrossRef Medline

71. Zihni, C., Vlassaks, E., Terry, S., Carlton, J., Leung, T. K. C., Olson, M., Pichaud, F., Balda, M. S., and Matter, K. (2017) An apical MRCK-driven morphogenetic pathway controls epithelial polarity. *Nat. Cell Biol.* **19,** 1049–1060 CrossRef Medline
72. Yeaman, C., Grindstaff, K. K., and Nelson, W. J. (2004) Mechanism of recruiting Sec6/8 (exocyst) complex to the apical junctional complex during polarization of epithelial cells. *J. Cell Sci.* **117,** 559–570 CrossRef Medline
73. Rodríguez-Fraticelli, A. E., Bagwell, J., Bosch-Fortea, M., Boncompain, G., Reglero-Real, N., García-León, M. J., Andrés, G., Toribio, M. L., Alonso, M. A., Millán, J., Perez, F., Bagnat, M., and Martín-Belmonte, F. (2015) Developmental regulation of apical endocytosis controls epithelial patterning in vertebrate tubular organs. *Nat. Cell Biol.* **17,** 241–250 CrossRef Medline
74. Crawley, S. W., Shifrin, D. A., Jr., Grega-Larson, N. E., McConnell, R. E., Benesh, A. E., Mao, S., Zheng, Y., Zheng, Q. Y., Nam, K. T., Millis, B. A., Kachar, B., and Tyska, M. J. (2014) Intestinal brush border assembly driven by protocadherin-based intermicrovillar adhesion. *Cell* **157,** 433–446 CrossRef Medline
75. Shen, L., Weber, C. R., and Turner, J. R. (2008) The tight junction protein complex undergoes rapid and continuous molecular remodeling at steady state. *J. Cell Biol.* **181,** 683–695 CrossRef Medline
76. Clayburgh, D. R., Barrett, T. A., Tang, Y., Meddings, J. B., Van Eldik, L. J., Watterson, D. M., Clarke, L. L., Mrsny, R. J., and Turner, J. R. (2005) Epithelial myosin light chain kinase-dependent barrier dysfunction mediates T cell activation-induced diarrhea *in vivo*. *J. Clin. Invest.* **115,** 2702–2715 CrossRef Medline
77. Barth, A. I., Pollack, A. L., Altschuler, Y., Mostov, K. E., and Nelson, W. J. (1997) NH_2-terminal deletion of beta-catenin results in stable colocalization of mutant β-catenin with adenomatous polyposis coli protein and altered MDCK cell adhesion. *J. Cell Biol.* **136,** 693–706 CrossRef Medline
78. Van Itallie, C. M., Fanning, A. S., Bridges, A., and Anderson, J. M. (2009) ZO-1 stabilizes the tight junction solute barrier through coupling to the perijunctional cytoskeleton. *Mol. Biol. Cell* **20,** 3930–3940 CrossRef Medline
79. Yu, A. S., McCarthy, K. M., Francis, S. A., McCormack, J. M., Lai, J., Rogers, R. A., Lynch, R. D., and Schneeberger, E. E. (2005) Knockdown of occludin expression leads to diverse phenotypic alterations in epithelial cells. *Am. J. Physiol. Cell Physiol.* **288,** C1231–C1241 CrossRef Medline
80. Buschmann, M. M., Shen, L., Rajapakse, H., Raleigh, D. R., Wang, Y., Wang, Y., Lingaraju, A., Zha, J., Abbott, E., McAuley, E. M., Breskin, L. A., Wu, L., Anderson, K., Turner, J. R., and Weber, C. R. (2013) Occludin OCEL-domain interactions are required for maintenance and regulation of the tight junction barrier to macromolecular flux. *Mol. Biol. Cell* **24,** 3056–3068 CrossRef Medline

The scaffolding protein ZO-1 coordinates actomyosin and epithelial apical specializations *in vitro* and *in vivo*

Matthew A. Odenwald, Wangsun Choi, Wei-Ting Kuo, Gurminder Singh, Anne Sailer, Yitang Wang, Le Shen, Alan S. Fanning and Jerrold R. Turner

J. Biol. Chem. 2018, 293:17317-17335.
doi: 10.1074/jbc.RA118.003908 originally published online September 21, 2018

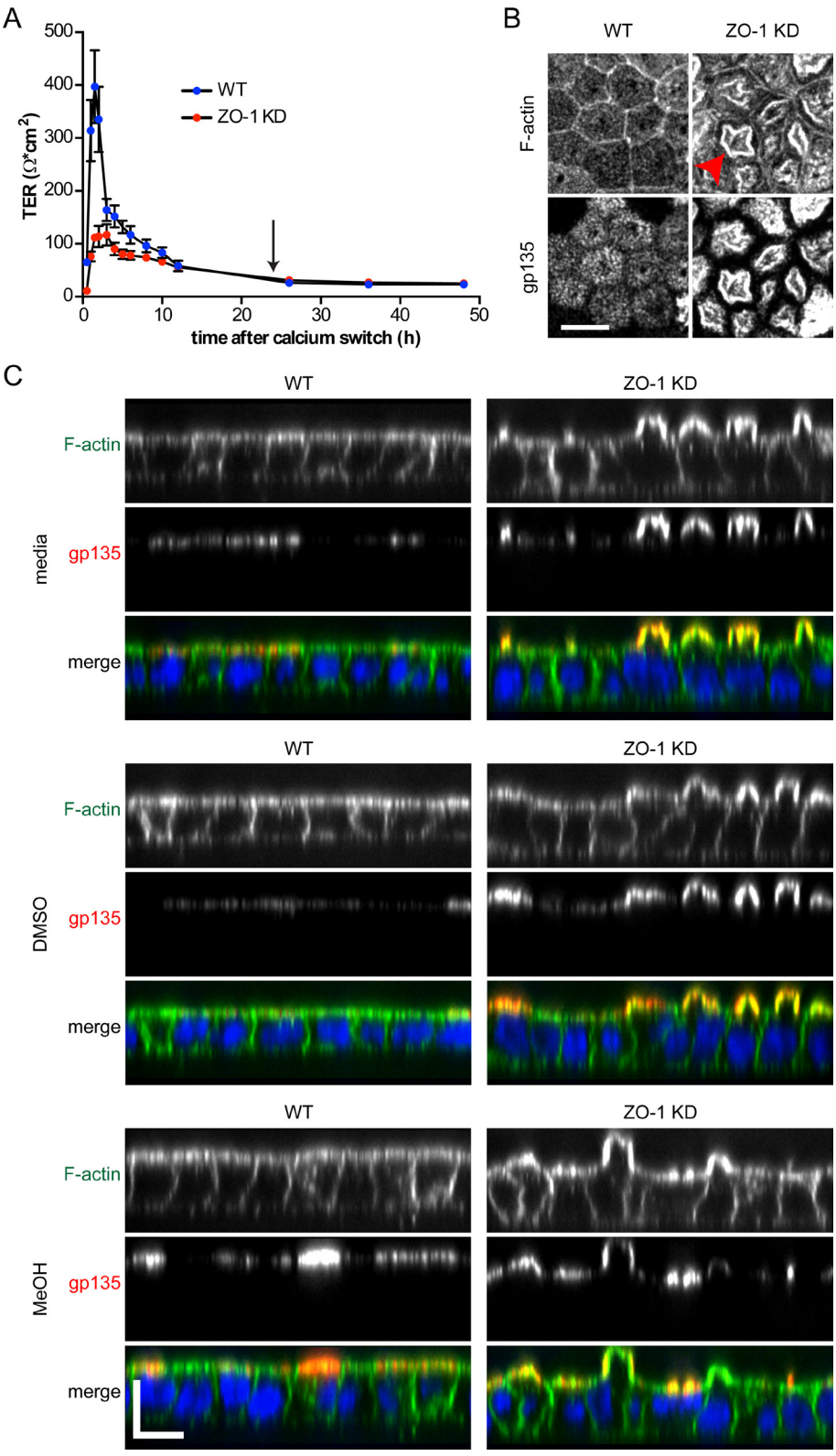

Supporting Information Figure S1. ZO-1 KD reduces, but does not delay, barrier development. (A) Confluent WT and ZO-1 KD monolayers were subjected to a calcium-switch assay. Development of monolayer barrier

function was measured as TER for 48 h after calcium repletion. Graph depicts mean±SD from one experiment representative of three independent trials, each performed in triplicate ($p<0.001$ by two-tailed t-test at peak TER). (B, C) Monolayers were immunostained for F-actin (phalloidin, green), podocalyxin/gp135 (red), and nuclei (Hoechst, blue) 24 hours after calcium repletion with either regular culture media or media containing either DMSO (1:300) or methanol (1:100) as vehicles. Representative maximal projections of full monolayer thickness *z*-stacks and *x,z* projections are shown. All images for a given antigen and image orientation are scaled identically. Bar = 10μm.

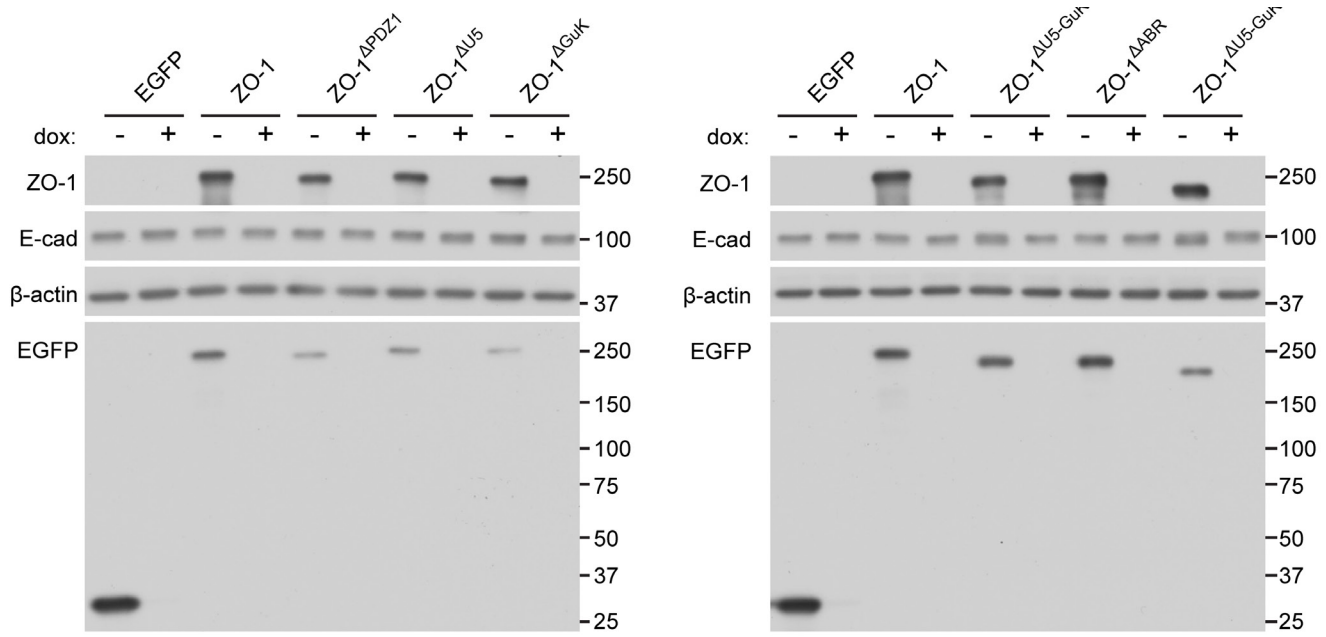

Supporting Information Figure S2. Inducible expression of ZO-1 mutants in ZO-1 KD epithelia. ZO-1 KD cells expressing either free EGFP or the indicated EGFP-tagged ZO-1 mutant were grown to confluence in the presence or absence of doxycycline to repress or induce transgene expression, respectively. Lysates were immunoblotted for ZO-1 and EGFP to confirm inducible expression of EGFP-tagged ZO-1 mutants. Lysates were probed for E-cadherin and β-actin as loading controls.

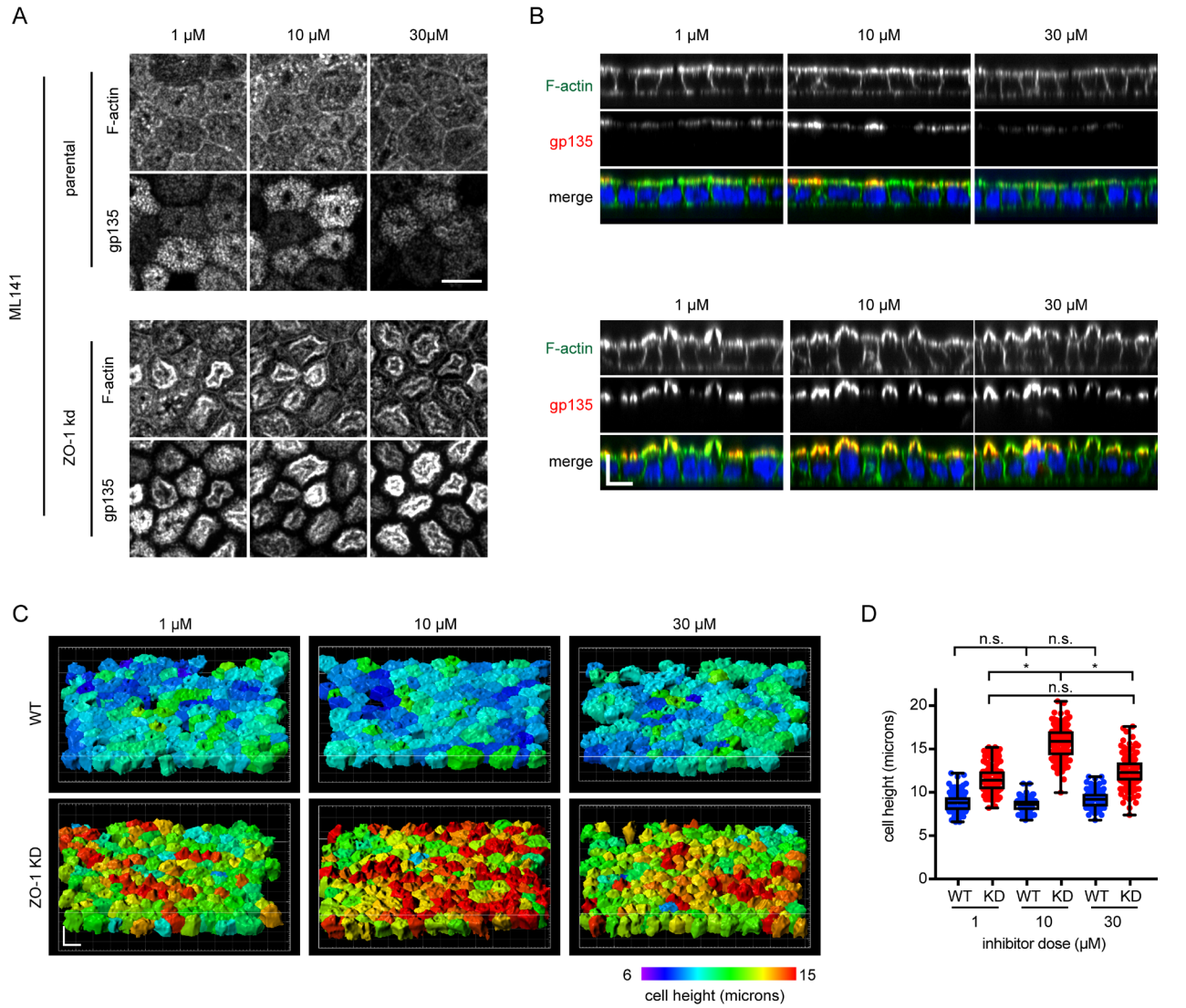

Supporting Information Figure S3. Cdc42 regulates cell height without affecting apical cell structure. (A, B) Confluent WT and ZO-1 KD monolayers were subjected to calcium-switch and treated with 1, 10, or 30 µM ML141 upon calcium repletion. Monolayers were then stained for F-actin (phalloidin, green), podocalyxin/gp135 (red), and nuclei (Hoechst, blue). Representative maximal projections of full monolayer thickness *z*-stacks and *x,z* projections are shown. All images for a given antigen are scaled identically. Bar = 10µm. (C) 3D renderings of individual cells were generated using F-actin as a membrane marker. Cells are colored based on cell height as indicated. Bar = 10 µM. (D) Height of each 3D cell rendering was determined. Box encloses 2nd and 3rd quartiles, center bar indicates the mean, bars extend to maximum and minimum values. Data are from one experiment representative of three independent studies. In this experiment, WT, n = 143, 123, and 128; KD, n = 151, 171, and 188 for 1µM, 3µM, and 10µM, respectively. n.s., $p>0.05$ and *, $p<0.001$ by one way ANOVA with Kruskal-Wallis post-test for comparison indicated by brackets.

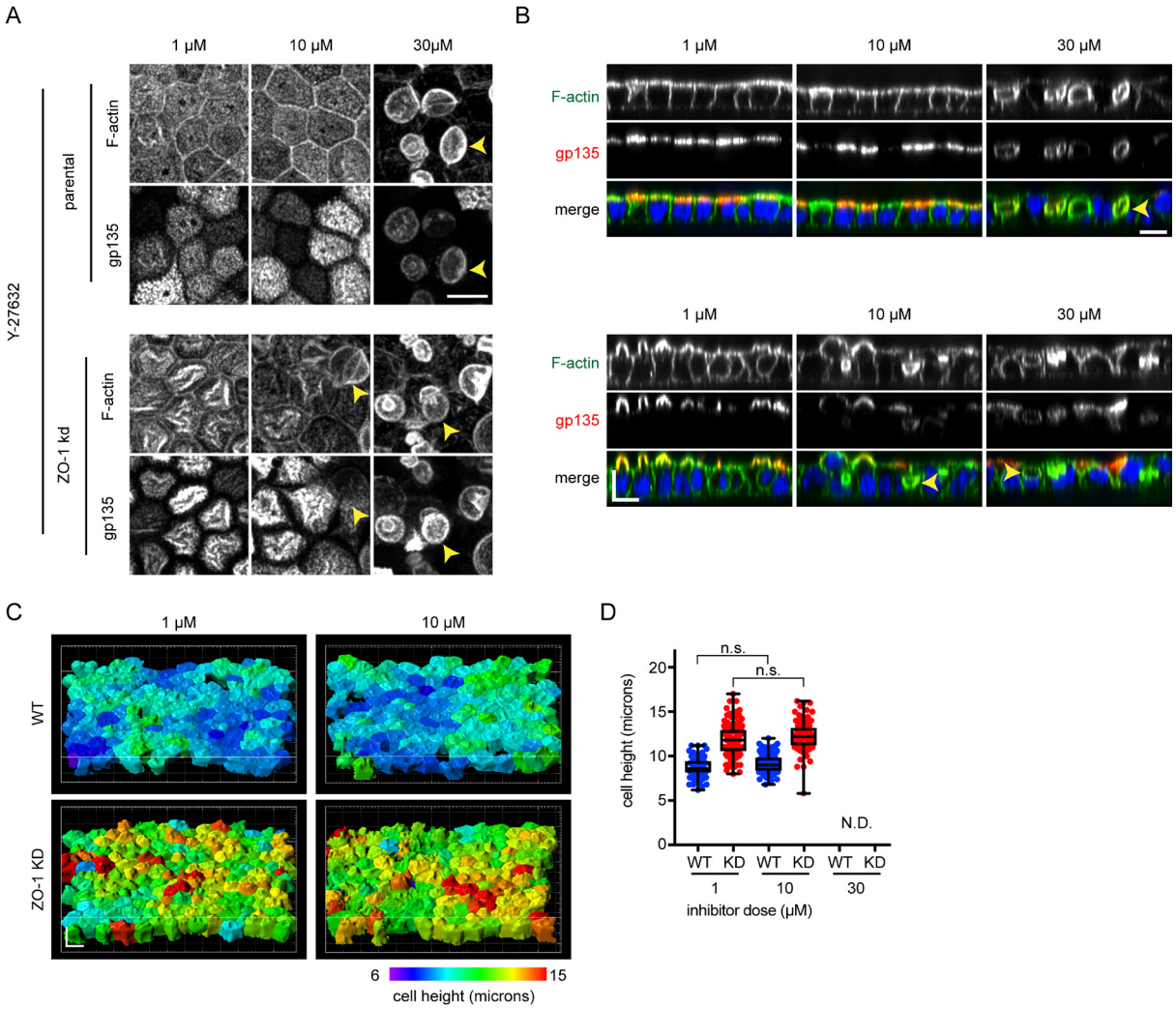

Supporting Information Figure S4. Rho kinase activity is essential for monolayer polarization and apical cell structure. (A, B) Confluent WT and ZO-1 KD monolayers were subjected to calcium-switch and treated with 1 μM, 10 μM, or 30 μM Y-27632 upon calcium repletion. Monolayers were then stained for F-actin (phalloidin, green), podocalyxin/gp135 (red), and nuclei (Hoechst, blue). Representative maximal projections of full monolayer thickness *z*-stacks and *x,z* projections are shown. All images for a given antigen are scaled identically. Bar = 10μm. (C) 3D renderings of individual cells were generated using F-actin as a membrane marker. Cells could not be created at the highest dose of Y-27632 (30 μM) due to marked disruption of F-actin. Cells are colored based on cell height as indicated. Bar = 10 μm. (D) Height of each 3D cell rendering was determined. Box encloses 2nd and 3rd quartiles, center bar indicates the mean, bars extend to maximum and minimum values. Data are from one experiment representative of three independent studies. In this experiment, WT, n = 163 and 138; KD, n =181 and 152 for 1μM and 10μM, respectively. n.s., p>0.05 by one way ANOVA with Kruskal-Wallis post-test for comparison indicated by brackets.

Supporting Information Table 1. Antibodies used.

Antigen	Species	Source	Dilution (IF)	Dilution (WB)
α-catenin	rabbit	Cell Signaling (3236)	1:100	1:1,000
β-actin	mouse	Sigma-Aldrich (clone AC-15, A1978)	N/A	1:10,000
E-cadherin	rabbit	Cell Signaling (clone 24E10, 3195S)	1:100	1:10,000
E-cadherin	Mouse	Abcam (ab76055)	1:100	N/A
GFP	mouse	clone F56-6A.1.23 (culture supernatant)	1:1	1:1,000
gp135	mouse	clone 3F2/D8	1:100	N/A
myosin IIB	rabbit	BioLegend (PRB-445P)	1:100	N/A
occludin	mouse	Invitrogen (33-1500)	1:100	1:1,000
NHE3	rabbit	Abcam (ab101817)	2.5 μg/ml	N/A
PKC-ζ	rabbit	Sigma-Aldrich (P0713)	1:100	N/A
ZO-1	rat	clone R40.76 (culture supernatant)	1:2	1:5
ZO-1	mouse	Invitrogen (33-9100)	1:100	1:1,000
ZO-2	mouse	Invitrogen (374700)	1:100	1:1,000

Supporting Information Table 2. Inhibitors used in calcium switch studies

Inhibitor	Source (Catalog #)	Solvent	Stock concentration
BDM	Sigma-Aldrich (B0753)	Methanol	1 M
blebbistatin	Sigma-Aldrich (B0560)	DMSO	10 mM
dynasore	Sigma-Aldrich (D7693)	DMSO	30 mM
latrunculin A	Life Technologies (L12370)	DMSO	1 mM
ML141	Sigma-Aldrich (SML0407)	DMSO	10 mM
Y-27632	Fisher (NC0407157)	Water	50 mM

Supporting Video S1: **ZO-1 is essential for formation of a uniform epithelial apical surface *in vivo.*** Whole mount sections of jejunum epithelium from WT and ZO-1 KO mice were fixed and stained for F-actin (phalloidin) and nuclei (Hoechst). The full thickness of each monolayer was imaged with confocal microscopy, and *z*-stacks were reconstructed to create the three different views of each representative WT (top) and ZO-1 KO (bottom) whole mount shown in the video. The first view is a full volume view of F-actin (green) and nuclei (blue) fluorescence. Next, F-actin staining was used as a membrane marker to render a 3D volume of each cell (colored randomly). Finally, the apical surface of each monolayer was rendered using apical F-actin fluorescence. The whole mounts shown in this video are representative of whole mounts taken from 3 mice in independent experiments.

Supporting Video S2: **ZO-1 regulates F-actin organization and uniform apical surface development in epithelial monolayers.** Confluent WT and ZO-1 KD monolayers were subjected to calcium switch, and cells were fixed and stained for F-actin (phalloidin) 24 hours after calcium repletion. The full thickness of each monolayer was imaged with confocal microscopy, and *z*-stacks were reconstructed to create the four different views of each representative WT (top) and ZO-1 KD (bottom) monolayer shown in the video. The first view is a full volume view of F-actin fluorescence (green). The second view is also a full volume view that is pseudocolored based on F-actin fluorescence intensity as indicated. Fluorescence intensities are scaled identically in both WT and KD monolayers throughout the video. Third, F-actin staining was used as a membrane marker to render a 3D volume of each cell (colored randomly). Finally, the apical surface of each monolayer was rendered using apical F-actin fluorescence. The monolayers shown in this video are representative of >3 independent experiments with at least n=3 for each condition. Bar = 20μm throughout the video.